TECHNISCHE UNIVERSITÄT WIEN

Master Thesis

Analysis of the Efficient Induction Heating Frequency

carried out for the purpose of obtaining the degree of
Diplom-Ingenieur (Dipl.-Ing.)

submitted at TU Wien
Faculty of Mechanical and Industrial Engineering
by

Ben HEINRICH

Mat.No.: 11826363

under the supervision of
Assistant Prof. Dipl.-Ing. Dr.techn. Florian Toth
and
Univ.Ass. Vladimir Filkin, MSc
Institute of Mechanics und Mechatronics, E325

Vienna, 22nd August 2023

Signature

I confirm, that the printing of this thesis requires the approval of the examination board.

Affidavit

I declare in lieu of oath, that I wrote this thesis and carried out the associated research myself, using only the literature cited in this volume. If text passages from sources are used literally, they are marked as such.

I confirm that this work is original and has not been submitted for examination elsewhere, nor is it currently under consideration for a thesis elsewhere. I acknowledge that the submitted work will be checked electronically-technically using suitable and state-of-the-art means (plagiarism detection software). On the one hand, this ensures that the submitted work was prepared according to the high-quality standards within the applicable rules to ensure good scientific practice "Code of Conduct" at the TU Wien. On the other hand, a comparison with other student theses avoids violations of my personal copyright.

Vienna, 22nd August 2023

Signature

Acknowledgements

I would like to express my gratitude to Assistant Prof. Dipl.-Ing. Dr.techn. Florian Toth and Univ.Ass. Vladimir Filkin, MSc for their guidance and advice during the whole research work. Appreciation is also extended to the members of the research unit Sensor and Actuator Technology who helped me whenever necessary and who created a positive working atmosphere. Finally, I would like to thank my parents and Lena Wild who supported me during my studies.

Contents

Abstract

The heating of metal sheets is an important industrial process with various applications, e.g., for the coating and drying of sheets, heat treatments or hot-forming. For these applications, induction heating offers an efficient and clean way to generate the required heat from electrical energy directly inside the sheet. Depending on the orientation of the magnetic field, one distinguishes between longitudinal flux heating, where the magnetic flux is tangential to the sheet surface, and transverse flux heating, where the magnetic flux is normal to the sheet surface. In both configurations, an important design parameter is the frequency of the alternating coil current that creates the time varying magnetic field. Given that the frequency selection drastically affects the system efficiency, this thesis investigates the choice of the optimal frequency to obtain maximum electrical efficiency.

To start with, important physical and numerical concepts related to the efficient simulation of induction heating applications will be reviewed. Even though no general three-dimensional analytical solutions are available for sheets due to the absence of rotational symmetries, different two-dimensional approaches will be introduced to gain a deeper understanding of the frequency dependency of the efficiency. Afterwards, two- and three-dimensional numerical results obtained with the Finite Element Method will be compared for both longitudinal and transverse flux heating. Here, investigating the validity of the computationally economical two-dimensional simulations will be of central importance. Moreover, the most important geometry and material parameters will be identified and their influence on optimal frequency and efficiency will be analyzed.

Nomenclature

Acronyms

AC Alternating Current
BC Boundary Condition
DC Direct Current
DOF Degree Of Freedom
FEM Finite Element Method
LFH Longitudinal Flux Heating
PDE Partial Differential Equation
rms root mean square
TFH Transverse Flux Heating

Symbols

$\boldsymbol{E}$	V/m	electric field intensity
$\boldsymbol{D}$	As/m^2	electric flux density
$\boldsymbol{J}$	A/m^2	current density
q_e	As/m^3	charge density
$\boldsymbol{H}$	A/m	magnetic field intensity
$\boldsymbol{B}$	T	magnetic flux density
$\boldsymbol{v}$	m/s	velocity of the heated body
$\boldsymbol{A}$	Tm	magnetic vector potential
V	V	electric scalar potential
μ	Vs/Am	magnetic permeability
μ_0	Vs/Am	vacuum permeability $\mu_0 \approx 4\pi \times 10^{-7}$Vs/Am
μ_r	-	relative magnetic permeability
ν	Am/Vs	magnetic reluctivity
ϵ	As/Vm	electric permittivity
γ	1/Ωm	electric conductivity
f	Hz	frequency
ω	1/s	angular frequency
ϑ	°C	temperature
ρ	kg/m^3	density
c_p	J/(kgK)	heat capacity
λ	W/(mK)	heat conductivity
P	W	(active) power
U	V	voltage
I	A	electric current
η	-	(electrical) efficiency

Chapter 1

Introduction

In view of the urgent need to decarbonize industrial heating processes, induction heating is a key technology. Induction heating uses an inductor coil excited by alternating current (AC) to induce currents in a conductive material and thereby produces heat inside the material through resistive losses. In comparison to other electro-heat technologies, e.g., resistance furnaces, the electrical energy is used for heat generation in a more efficient way: the heat is produced directly inside the target without any contact between target and heating installation. Thus, heat losses to the environment are reduced and high efficiency of the energy transformations can be achieved. Additionally, the rapid thermal start-up of the installations saves energy in situations with varying production rates. Accurate control and excellent repeatability of the process, combined with short heating times due to high power densities, allow full automation with a small number of rejected workpieces, saving both resources and labor costs [1] [2].

This thesis focuses on the continuous heating of metal sheets. This procedure is used in numerous processes and comprises coating and drying of sheets, heat treatments as well as intermediate heating before milling. Accordingly, the desired temperature increases range from a few 10°C to 1200°C for hot-forming [3]. While design techniques for induction furnaces have been established since the early 1900s, the complete modelling of sheet heating processes is more challenging. First guidelines were developed around 1950 [4] [5], but only with the development of advanced numerical tools and improved power electronics the full potential of the heating setups could be exploited [2].

In that context, the frequency selection is of major importance, since it gives the possibility to control the eddy current distribution inside the heated body and strongly affects the efficiency of the process. This thesis aims at analyzing the most efficient coil excitation frequency for the induction heating of metal sheets. In Chapter 2, we will introduce important concepts of electromagnetism and thermodynamics needed for the understanding of the underlying physics. Furthermore, the two major setups for sheet induction heating treated in this thesis are introduced. From a numerical point of view, the coupled electromagnetic-heat problem is solved by the Finite Element Method (FEM). In this thesis, openCFS [6], an open-source finite element-based multi-physics modelling and simulation tool, is used. For the efficient simulation of electromagnetic phenomena in the context of induction heating, a number of specific numerical techniques is required and will be presented in Chapter 3. Even though no complete analytical solutions for general three-dimensional sheet induction heating setups are available, Chapter 4 deals with a number of analytical approaches, which are useful for a qualitative understanding of the frequency dependency of the efficiency and can help to interpret the simulation results. In Chapter 5, efficiency curves over frequency for two- and three-dimensional simulations will be discussed. Chapter 6 investigates the influence of different geometrical and material parameters on the efficiency and the optimal frequency.

Chapter 2

Induction Heating: Physical and Technical Basics

2.1 Electromagnetic Field

To understand how the currents are induced in the sheet and how their distribution depends on the frequency, a good understanding of the underlying principles is necessary. Hence, the following section aims at giving a short introduction to important electrodynamic concepts. The naming conventions from [7] and [8] will be adopted.

The electric and magnetic fields are described by the Maxwell equations [9]

$$\nabla \times \boldsymbol{H} = \boldsymbol{J} + \frac{\partial \boldsymbol{D}}{\partial t}, \tag{2.1}$$

$$\nabla \times \boldsymbol{E} = -\frac{\partial \boldsymbol{B}}{\partial t}, \tag{2.2}$$

$$\nabla \cdot \boldsymbol{D} = q_e, \tag{2.3}$$

$$\nabla \cdot \boldsymbol{B} = 0. \tag{2.4}$$

The generalized Ampère's law (2.1) states that a time variable electric field or a stationary current density causes a magnetic field. According to Faraday's law (2.2), a magnetic field changing with time produces an electric field. Gauss' law (2.3) introduces the stationary electric charge as a source for the electric field, while (2.4) prohibits the existence of stationary sources for the magnetic field.

In isotropic, linear materials the constitutive relations read

$$\boldsymbol{J} = \gamma(\boldsymbol{E} + \boldsymbol{v} \times \boldsymbol{B}), \tag{2.5}$$

$$\boldsymbol{D} = \epsilon \boldsymbol{E}, \tag{2.6}$$

$$\boldsymbol{B} = \mu \boldsymbol{H} = \mu_r \mu_0 \boldsymbol{H}. \tag{2.7}$$

In the general case, polarization and magnetization must be included. For small values of the magnetic field intensity $\boldsymbol{H}$, (2.7) is a linear relation. For ferromagnetic materials, there is a nonlinear relation between $\boldsymbol{B}$ and $\boldsymbol{H}$ leading to the hysteresis curve. Further details can be found, e.g., in [10]. The electric conductivity γ, the electric permittivity ϵ and the magnetic permeability μ are scalars only for homogeneous isotropic media, while in general, they are tensors. In this thesis linear isotropic media are assumed.

Two electrodynamic potentials can be derived using the vector calculus identities for an arbitrary scalar φ and a vector $\boldsymbol{u}$ [11]

$$\nabla \times (\nabla \varphi) = \mathbf{0}, \tag{2.8}$$

$$\nabla \cdot (\nabla \times \boldsymbol{u}) = 0. \tag{2.9}$$

Since the $\boldsymbol{B}$ field must be divergence free according to (2.4), (2.9) can be used to define a magnetic vector potential $\boldsymbol{A}$

$$\boldsymbol{B} = \nabla \times \boldsymbol{A}. \tag{2.10}$$

Inserting this relation in (2.2) yields

$$\nabla \times \left(\boldsymbol{E} + \frac{\partial \boldsymbol{A}}{\partial t} \right) = 0, \tag{2.11}$$

while from (2.8) another scalar potential can be introduced. The so-called electric scalar potential V is defined as

$$\boldsymbol{E} = -\nabla V - \frac{\partial \boldsymbol{A}}{\partial t}. \tag{2.12}$$

Now the solution of the Maxwell equations is reduced to the computation of four field components. However, these potentials are not unique. In fact, they can be modified with an arbitrary scalar function Λ depending on time and space without changing the actual values of $\boldsymbol{B}$ and $\boldsymbol{E}$

$$\boldsymbol{A}' = \boldsymbol{A} - \nabla \Lambda, \tag{2.13}$$

$$V' = V + \frac{\partial \Lambda}{\partial t}. \tag{2.14}$$

This is a problem of the Gauge theory, which is described in depth in [11]. The so-called Coulomb gauge

$$\nabla \cdot \boldsymbol{A} = 0, \tag{2.15}$$

is commonly used as an additional constraint to assure uniqueness. This is verified automatically in the two-dimensional or axisymmetric case. Moreover, it is not necessary to explicitly impose this constraint if we are only interested in the $\boldsymbol{B}$ field [7]. Another advantage is that V can be determined with the methods of electrostatics even for time-dependent problems, because the equations for $\boldsymbol{A}$ and V decouple [11]. In computational electromagnetics, the temporal gauge which consists of setting $V = 0$ is also commonly used [12].

For induction heating, the displacement currents are neglected, because at low frequencies smaller than those of the optical spectrum the dimensions of the studied regions are small compared to the electromagnetic wavelengths [13]. In that case, the set of Maxwell equations (2.1) and (2.2) can be combined with the constitutive laws (2.5) and (2.7) to the curl-curl equation for the magnetic vector potential [7]

$$\nabla \times \nu \nabla \times \boldsymbol{A} = \boldsymbol{J}_\mathrm{i} - \gamma \frac{\partial \boldsymbol{A}}{\partial t} + \gamma (\boldsymbol{v} \times \nabla \times \boldsymbol{A}). \tag{2.16}$$

Here $\boldsymbol{J}_\mathrm{i}$ represents the impressed current density, e.g., through current or voltage excitation and $\nu = 1/\mu$ is the magnetic reluctivity. The velocity term is neglected in the following. Note that for the eddy current problem, $\boldsymbol{E}$ denotes the solenoidal part $\boldsymbol{E}_\mathrm{s}$ of the electric field intensity, obtained through the Helmholtz decomposition of $\boldsymbol{E}$ into a solenoidal $\boldsymbol{E}_\mathrm{s}$ and an irrotational part $\boldsymbol{E}_\mathrm{i}$, $\boldsymbol{E} = \boldsymbol{E}_\mathrm{s} + \boldsymbol{E}_\mathrm{i}$. The irrotational part is associated with the impressed current density $\boldsymbol{J}_\mathrm{i}$.

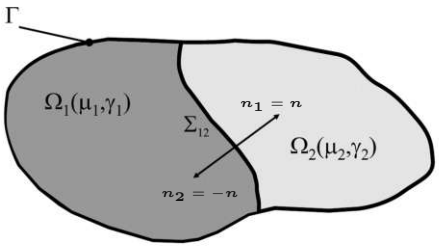

Figure 2.1: Interface between 2 domains with different material properties, image taken from [7].

Industrial settings often involve several materials with different magnetic or electric properties. Thus, it is important to know how the electromagnetic field quantities behave at the interface between different media. Let us consider the two domains Ω_1 and Ω_2 shown in Fig. 2.1, sharing a common interface. Field values in the different domains are denoted by the respective index 1 or 2. The common normal vector of the interface is denoted by $\boldsymbol{n}$. The interface conditions can be derived by applying Gauss' or Stoke's theorem to the integral forms of the Maxwell equations. Details on this procedure can be found in [7] or [10].
From (2.4) follows the continuity of the normal component of $\boldsymbol{B}$

$$\boldsymbol{n} \cdot (\boldsymbol{B}_1 - \boldsymbol{B}_2) = 0 \implies B_{1n} = B_{2n}, \tag{2.17}$$

where the index n represents the normal component of the magnetic flux density at the interface. When there is no surface current present, (2.1) results in the continuity of the tangential component of $\boldsymbol{H}$

$$\boldsymbol{n} \times (\boldsymbol{H}_1 - \boldsymbol{H}_2) = \boldsymbol{0} \implies H_{1t} = H_{2t}, \tag{2.18}$$

with the index t indicating the tangential component of the magnetic field intensity at the interface. In the absence of a time-varying magnetic field, it can be shown from (2.2) that the tangential component of $\boldsymbol{E}$ is also continuous across boundaries.
Taking the divergence of (2.1), one can show by using identity (2.9) that the normal component of $\boldsymbol{J}$ must be continuous

$$\nabla \cdot \boldsymbol{J} = 0 \implies J_{1n} = J_{2n}. \tag{2.19}$$

2.2 Skin Effect

At higher frequencies, the current density is not homogeneous over the cross section of a conductor, but is concentrated at the surface and strongly decreases towards the internal part of the conductor. The reason is the self induction of the conductor: according to Lenz's law, the induced secondary current is directed in the same direction as the primary current at the conductor surface while the induced current flows in the opposite direction in the internal part [14].

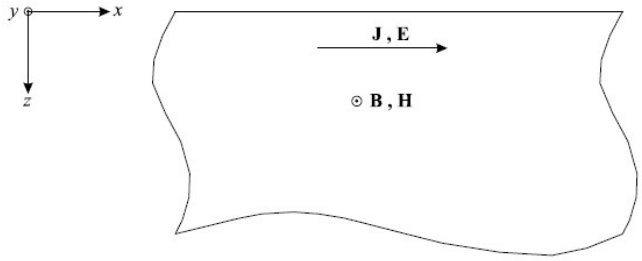

Figure 2.2: Infinite half plane for the derivation of the skin effect, image taken from [7].

For the infinite half plane shown in Fig. 2.2, the skin effect can be derived analytically, following [7]. The electric field quantities are directed in x direction, while the magnetic field quantities are oriented along the y-axis. There are spatial dependencies on the z-coordinate only. (2.1) and (2.2) reduce to:

$$-\frac{\partial H_y}{\partial z} = J_x = \gamma E_x \tag{2.20}$$

$$\frac{\partial E_x}{\partial z} = -\frac{\partial B_y}{\partial t} = -\mu \frac{\partial H_y}{\partial t} \tag{2.21}$$

For a harmonic excitation with angular frequency $\omega = 2\pi f$, the equations can be transformed to the frequency domain. Thus the following diffusion equation is obtained for the complex amplitude $\hat{H}_y$ by combining (2.20) and (2.21)

$$\frac{\partial^2 \hat{H}_y}{\partial z^2} = \mathrm{j}\omega\gamma\mu\hat{H}_y = k^2\hat{H}_y, \tag{2.22}$$

with $k^2 = \mathrm{j}\omega\gamma\mu$. The general ansatz for this differential equation is

$$\hat{H}_y(z) = C_1 e^{kz} + C_2 e^{-kz}. \tag{2.23}$$

Knowing that $\hat{H}_y$ must decrease with increasing distance from the surface z, $C_1 = 0$ and with the boundary condition at the plane surface $\hat{H}_y(z = 0) = H_0$, one obtains

$$\hat{H}_y(z) = H_0 e^{-kz}. \tag{2.24}$$

Defining the so-called skin penetration depth δ as

$$\delta = \frac{1}{\sqrt{\pi f \gamma \mu}}, \tag{2.25}$$

the solution for H_y can be written as

$$H_y(z, t) = H_0 e^{-z/\delta} \cos(\omega t - z/\delta). \tag{2.26}$$

The solutions for B_y, E_x and J_y have the same form as (2.26). Hence, we can conclude that the skin effect causes an exponential decay of the amplitude and an increase in the phase shift in the internal part of the conductor. The skin depth δ gives the distance from the surface at which the amplitude of the electromagnetic field quantities decreased by a factor $1/e$. It depends both on the material parameters and the frequency and is of major importance in induction heating because it gives an indication of the distribution of power sources in the heated material. As a matter of fact, 86% of the Joule losses are dissipated in the skin depth [15].

2.3 Heat Equation

To get the temperature distribution in the sheet, the heat conduction in the material, and the heat transfer at the sheet surface have to be modelled. In the following, the partial differential equation (PDE) for the space-and time dependent temperature $\vartheta(\boldsymbol{x}, t)$ will be derived and the relevant boundary conditions will be stated following [16]. The movement of the sheet with velocity $\boldsymbol{v}$ can be taken into account by a convective term, as shown in [17]. To derive this term we can use the Reynold's transport theorem for a moving material volume in the first law of thermodynamics [18]. The first law of thermodynamics for the closed system Ω with boundary Γ is given by

$$\frac{\mathrm{d}U}{\mathrm{d}t} = \dot{Q}(t) + P(t), \tag{2.27}$$

where the change in the total internal energy U is caused by the heat flux Q and the electrical or mechanical power P. Note that the variation of the specific internal energy with temperature can be expressed via the specific heat capacity c_p,

$$\mathrm{d}u = c_p(\vartheta)\mathrm{d}\vartheta. \tag{2.28}$$

For an incompressible volume, the density ρ is constant. Now the Reynold's transport theorem can be applied to compute the time derivative of the total internal energy of the moving body and we can use (2.28) to substitute the specific internal energy u,

$$\frac{\mathrm{d}U}{\mathrm{d}t} = \frac{\mathrm{d}}{\mathrm{d}t}\int_\Omega \rho u \,\mathrm{d}\Omega = \int_\Omega \frac{\partial(\rho u)}{\partial t} + \nabla\cdot(\rho u \boldsymbol{v})\,\mathrm{d}\Omega = \rho\int_\Omega c_p\frac{\partial\vartheta}{\partial t} + \nabla\cdot(c_p\vartheta\boldsymbol{v})\,\mathrm{d}\Omega. \tag{2.29}$$

According to Fourier's law, the heat flux density flowing into Ω for a heat conductivity $\lambda(\vartheta)$ is given by

$$\mathrm{d}\dot{Q} = -\dot{\boldsymbol{q}}\boldsymbol{n}\mathrm{d}\Gamma = \lambda(\vartheta)\nabla\vartheta\boldsymbol{n}\mathrm{d}\Gamma. \tag{2.30}$$

The negative sign comes from the convention that the normal vector $\boldsymbol{n}$ is oriented outwards. The total heat flux is obtained from integration over the surface and application of the Gauss' theorem to obtain a volume integral,

$$\dot{Q} = \int_\Gamma -\dot{\boldsymbol{q}}\boldsymbol{n}\,\mathrm{d}\Gamma = \int_\Omega \nabla\cdot(\lambda\nabla\vartheta)\,\mathrm{d}\Omega. \tag{2.31}$$

In induction heating, the power P is the dissipative power due to Joule losses in the conductor. Defining a volumetric heat source $\dot{q}_v$, P can be written as

$$P = \int_\Omega \dot{q}_v\,\mathrm{d}\Omega. \tag{2.32}$$

Assuming a constant c_p, 2.27 can be rewritten as

$$\rho c_p\int_\Omega\left(\frac{\partial\vartheta}{\partial t} + \nabla\cdot(\vartheta\boldsymbol{v})\right)\mathrm{d}\Omega = \int_\Omega \nabla\cdot(\lambda\nabla\vartheta)\,\mathrm{d}\Omega + \int_\Omega \dot{q}_v\,\mathrm{d}\Omega. \tag{2.33}$$

Finally, the heat conduction PDE for a body moving with velocity $\boldsymbol{v}$ states [19]

$$\rho c_p\left(\frac{\partial\vartheta}{\partial t} + \boldsymbol{v}\cdot\nabla\vartheta\right) = \nabla\cdot(\lambda\nabla\vartheta) + \dot{q}_v. \tag{2.34}$$

To obtain a unique temperature field, boundary conditions (BCs) have to be given at the surface Γ. One possibility is to set a fixed temperature $\vartheta(\boldsymbol{x}, t)$, e.g., at the inlet of the induction heater.

A prescribed heat flux $\hat{\boldsymbol{q}} = -\lambda \frac{\partial \vartheta}{\partial \boldsymbol{n}}$ is also possible, e.g., zero heat flux at the outlet of the induction heater. To model contact with a different medium, e.g., in the case of convective heat transfer at the surface of the sheet, a heat transfer BC can be stated. Then the heat flux is expressed as $\hat{\boldsymbol{q}} = \alpha(\vartheta - \vartheta_F)$, where α is the heat transfer coefficient for convection and ϑ_F is the bulk temperature of the surrounding fluid. In all these heat transfers, radiation is neglected.

2.4 Measures of Efficiency

The total efficiency of the induction heating process is the product of the electrical efficiency η_{el} and the thermal efficiency η_p [15],

$$\eta = \eta_{el} \cdot \eta_p. \tag{2.35}$$

The thermal efficiency mainly depends on the thermal isolation of the process and on the heating time t_1,

$$\eta_p = \frac{\int_0^{t_1} P_\mathrm{E}\,\mathrm{d}t - \int_0^{t_1} P_\mathrm{V}\,\mathrm{d}t}{\int_0^{t_1} P_\mathrm{E}\,\mathrm{d}t}, \tag{2.36}$$

where P_E is the power transferred to the heated body and P_V are the heat power losses, e.g., radiation or convection from the heated body or heat conduction to support structures [1]. η_p cannot be directly influenced by the frequency, thus only the electrical efficiency η_el will be considered in the following. We neglect the losses in all other electrical components, such as power converters or electric lines, as well as eddy current losses in electrically conductive bodies in the vicinity of the inductor, e.g., metal support beams, considering only the efficiency of the inductor-sheet system [1][8]. We then arrive at

$$\eta_\mathrm{el} = \frac{P_\mathrm{Joule}}{P_\mathrm{Joule} + P_\mathrm{Ind}} = \frac{P_\mathrm{Joule}}{P}, \tag{2.37}$$

where P_Joule are the Joule losses in the sheet acting as heat sources and P_Ind are the undesirable Joule losses in the inductor coil. For the definition of the active power P and all other characteristic alternating current AC quantities, we follow [20] and [21]. First we need to introduce the concept of root-mean-square (rms) quantities. The rms current is the constant direct current (DC) that dissipates the same power in a resistance than the alternating current over the same period. The same definition is valid for the rms value of voltage. In a general way, the rms value of an electric quantity u_rms over a period T can be computed by

$$u_\mathrm{rms} = \sqrt{\frac{1}{T}\int_0^T u^2(t)\,\mathrm{d}t} \tag{2.38}$$

The complex (rms) values of voltage $\hat{U}_\mathrm{rms}$ and current $\hat{I}_\mathrm{rms}$ for sinusoidal conditions can be computed from their respective complex amplitudes $\hat{U}$ and $\hat{I}$ by $\hat{U}_\mathrm{rms} = \hat{U}/\sqrt{2}$ and $\hat{I}_\mathrm{rms} = \hat{I}/\sqrt{2}$. The complex power $\hat{S}$ is defined as

$$\hat{S} = \hat{U}_\mathrm{rms}\hat{I}^*_\mathrm{rms}, \tag{2.39}$$

where * denotes the complex conjugate. The amplitude $||\hat{S}||$ of $\hat{S}$ is called apparent power. The real part of $\hat{S}$ is called active power $P = Re(\hat{S})$ and its complex part is referred to as reactive power $Q = Im(\hat{S})$. The power factor $\cos(\varphi)$ is given by

$$\cos(\varphi) = \frac{P}{||\hat{S}||}. \tag{2.40}$$

A high value of the power factor is another important criterion for the selection of the optimum frequency [22], because the electrical system has to be designed for the apparent power, while only the active power P generates heat.

2.5 Induction Heating Setups for Sheets

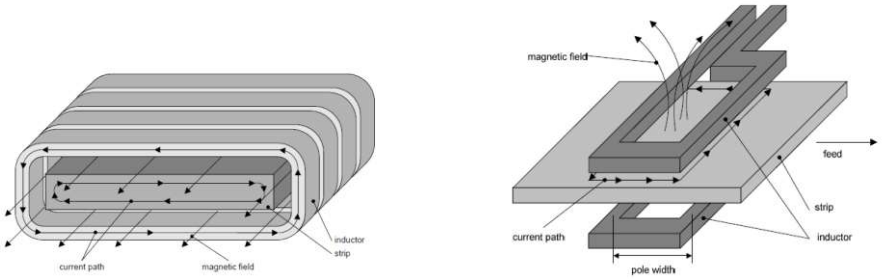

(a) Longitudinal flux heating (b) Transverse flux heating

Figure 2.3: Induction heating setups for metal sheets, images taken from [23].

There are 2 possibilities to arrange the inductor for the induction heating of metal sheets: the sheet can be completely surrounded by the inductor (Longitudinal Flux Heating, LFH), shown in Fig. 2.3(a)) or the inductor can be parallel to the sheet surface (Transverse Flux Heating, TFH), shown in Fig. 2.3(b)). The respective names come from the direction of the magnetic field penetrating the sheet: in the longitudinal case, it is oriented parallel to the sheet surface, while in the transverse case it is normal to the sheet surface. The current path in the sheet is the "image" of the currents in the inductor, as can be seen from Fig. 2.3.

In the longitudinal setup, a homogenous heating of the sheet is achieved. Contrarily, for the transverse setup the current paths are concentrated at the sheet edges, as they have to change their direction along the edge, causing higher Joule losses in this region. To achieve a homogeneous target temperature distribution, the shape and dimensions of the inductor have to be adapted accordingly. In many cases numerical simulations and optimization algorithms are applied to realize a certain temperature distribution [3]. Still, the edge overheating problematic is one of the major disadvantages of TFH compared to LFH [24]. Even when a certain optimal geometry has been found for achieving temperature uniformity, there is low flexibility to adapt it to sheets of different sizes. Furthermore, the non-uniform shape of the heating patter can produce significant mechanical deformation,vibration and noise. The aforementioned aspects will lead to high initial investment costs, since they require advanced design techniques and specialized electric components.

Empirically, good electrical efficiencies are achieved for LFH when choosing the ratio of sheet thickness d to penetration depth δ, d/δ, between 2.5 and 5. For TFH this ratio generally is only between 0.05 and 0.3 [15]. From the definition of the skin penetration depth, (2.25), we can see that for the same material parameters the ratio d/δ is proportional to $\sqrt{f}$, implying that in order to achieve optimal efficiency based on the previously mentioned criteria, the resulting frequency for LFH will be 1-2 orders of magnitude higher than for TFH. Hence, longitudinal flux heating is only used for sufficiently thick sheets or materials with high magnetic permeability. For thin non-magnetic sheets, frequencies in the range of radio-waves (>100kHz) are necessary. To produce such excitation frequencies, expensive power converters are necessary and there are significantly higher losses in the electronic switches of the power supply. Thus, for thin steel sheets, TFH has the advantage of a high electrical efficiency (up to 95%) using much lower frequencies [24]. At the same time, the reactive power is smaller [25].

Chapter 3

Numerical Methods for Induction Heating Applications

The numerical solution of induction heating problems with the FEM is challenging: For one thing, the eddy current problem needs to be solved in several domains with different permeability and conductivity, namely the inductor, the sheet and the surrounding air. The curl-curl nature of the eddy-current problem leads to issues, especially in 3D where the div-grad equation found in most applications modelled by FEM is fundamentally different from the curl-curl equation and requires different treatment [26]. Thus, besides deriving the weak formulation, we will need to have a close look at the requirements for the interpolation functions. Moreover, the skin depth needs to be sufficiently resolved, leading to large differences in mesh sizes between domains. Also, a proper excitation mode in the inductor is required, allowing for the efficient determination of current and voltage at the ports to compute the active input power. Finally, an efficient approach to couple the electromagnetic field computations to the heat equation in the sheet is needed. The notation in this chapter follows [7] and [8].

3.1 Weak Formulation of the Eddy Current Problem

To analyze the requirements on the approximation functions for the eddy current problem, we will first need to review some fundamental aspects of function spaces for FEM. In this regard, Sobolev spaces are a central concept. Generally, these spaces are vector spaces whose elements are functions defined on domains in $\mathbb{R}^n$ and whose partial derivatives satisfy certain integrability conditions [27]. They allow for studying "weak" solutions of PDEs in cases where the strong form of the PDE has no solution. The following definitions are taken from [27]. We consider a domain Ω in $\mathbb{R}^n$.
A differential operator of degree α is denoted by D^α, such that

$$D^\alpha = D^{\alpha_1} \cdots D^{\alpha_n} \qquad \text{with} \qquad D_j = \frac{\partial}{\partial x_j}. \tag{3.1}$$

Another important vector space is the Lebesgue space $L^p(\Omega)$ of all p-integrable functions that fulfill the condition

$$\int_\Omega |u(x)|^p \, \mathrm{d}x < \infty. \tag{3.2}$$

Before defining the Sobolev space, the concept of the weak derivative needs to be introduced. It extends the derivative in the classical sense to functions that are not smooth enough to have a continuous partial derivative of degree α. The weak derivative $D^\alpha u = v_\alpha$ is defined by

$$\int_\Omega u(x) D^\alpha \Phi(x)\,\mathrm{d}x = (-1)^{|\alpha|} \int_\Omega v_\alpha \Phi(x)\,\mathrm{d}x. \tag{3.3}$$

Finally, the Sobolev space $W^{m,p}(\Omega)$ is defined as

$$W^{m,p}(\Omega) = \{u \in L^p(\Omega), D^\alpha u \in L^p, \forall \alpha \leq m\}. \tag{3.4}$$

A Sobolev space with $p = 2$ is called Hilbert space and denoted by $H^m(\Omega)$.

Now we need to define a proper Sobolev space for finding a solution to the weak form of the curl-curl problem (2.16). A bounded domain has finite energy if the electromagnetic field quantities $\boldsymbol{E}$ and $\boldsymbol{H}$ are square-integrable. Thus, the L^2 space is an adequate choice [28]. We then define the functional space based on the curl operator, knowing that the rotor of the weak solution must be part of the chosen L^2 space. In the three-dimensional case it is defined in the general form as [28]

$$H(curl, \Omega) = \{\boldsymbol{u} \in L^2(\Omega)^3, \nabla \times \boldsymbol{u} \in L^2(\Omega)^3\}. \tag{3.5}$$

Now we can derive the weak formulation of the eddy current problem for the magnetic vector potential $\boldsymbol{A}$ following [7][8]. The computational domain Ω with boundary Γ is composed of the two subdomains Ω_1 and Ω_2, and share a common interface Σ. It is the same as for the derivation of interface conditions in Fig. 2.1. To start with, we reformulate the continuity conditions from Sec. 2.1 using $\boldsymbol{A}$

$$(2.17) \implies \boldsymbol{A}_1 \times \boldsymbol{n} = \boldsymbol{A}_2 \times \boldsymbol{n} \tag{3.6}$$

$$(2.18) \implies \nu_1 \boldsymbol{n} \times \nabla \times \boldsymbol{A}_1 = \nu_2 \boldsymbol{n} \times \nabla \times \boldsymbol{A}_1 \tag{3.7}$$

$$(2.19) \implies \gamma_1 \boldsymbol{n} \cdot \frac{\partial \boldsymbol{A}_1}{\partial t} = \gamma_2 \boldsymbol{n} \cdot \frac{\partial \boldsymbol{A}_2}{\partial t}. \tag{3.8}$$

Defining a jump operator for an arbitrary vector $\boldsymbol{u}$ as $[\boldsymbol{u}] = \boldsymbol{u}_1 - \boldsymbol{u}_2$, (3.6) can be rewritten as $[\boldsymbol{A} \times \boldsymbol{n}] = 0$. The requirement of divergence-free $\boldsymbol{B}$ field (2.4) gives the boundary condition

$$\boldsymbol{A} \times \boldsymbol{n} = \boldsymbol{0} \text{ on } \Gamma. \tag{3.9}$$

We now incorporate the above defined boundary condition on Γ and continuity condition on Σ into our functional space for $\boldsymbol{A}$, obtaining

$$H_0^\Sigma(curl, \Omega) = \{\boldsymbol{u} \in L^2(\Omega)^3, \nabla \times \boldsymbol{u} \in L^2(\Omega)^3, \boldsymbol{u} \times \boldsymbol{n}|_\Gamma = 0, [\boldsymbol{u} \times \boldsymbol{n}]\,|_\Sigma = 0\} \tag{3.10}$$

The strong form of the curl-curl problem 2.16 is multiplied with a vector valued test function $\boldsymbol{A}' \in H_0^\Sigma(curl, \Omega)$ to give

$$\int_\Omega \boldsymbol{A}' \cdot \nabla \times \nu \nabla \times \boldsymbol{A}\,\mathrm{d}\Omega + \int_\Omega \boldsymbol{A}' \cdot \gamma \frac{\partial \boldsymbol{A}}{\partial t}\,\mathrm{d}\Omega = \int_\Omega \boldsymbol{A}' \cdot \boldsymbol{J}_\mathrm{i}\,\mathrm{d}\Omega. \tag{3.11}$$

To transform this expression, Green's first integral theorem in vector form can be used

$$\int_\Omega (\nabla \times \boldsymbol{u} \cdot \nabla \times \boldsymbol{v} - \boldsymbol{u} \cdot \nabla \times \nabla \times \boldsymbol{v})\,\mathrm{d}\Omega = \int_\Gamma (\boldsymbol{u} \times \nabla \times \boldsymbol{v}) \cdot \boldsymbol{n}\,\mathrm{d}\Gamma. \tag{3.12}$$

From that, the final variational form can be written as: Find $\boldsymbol{A} \in H_0^{\Sigma}(curl, \Omega)$ such that

$$\int_{\Omega} \gamma \boldsymbol{A}' \cdot \frac{\partial \boldsymbol{A}}{\partial t} \, \mathrm{d}\Omega + \int_{\Omega} \nabla \times \boldsymbol{A}' \cdot \nu \nabla \times \boldsymbol{A} \, \mathrm{d}\Omega = \int_{\Omega} \boldsymbol{A}' \cdot \boldsymbol{J}_{\mathrm{i}} \, \mathrm{d}\Omega + \int_{\Gamma} (\boldsymbol{A}' \times \nu \nabla \times \boldsymbol{A}) \cdot \boldsymbol{n} \, \mathrm{d}\Gamma, \tag{3.13}$$

for any $\boldsymbol{A}' \in H_0^{\Sigma}(curl, \Omega)$. The boundary integral $\int_{\Gamma} (\boldsymbol{A}' \times \nu \nabla \times \boldsymbol{A}) \cdot \boldsymbol{n} \, \mathrm{d}\Gamma$ depends on the boundary condition and vanishes for (3.9).

From the interface conditions (3.6) and (3.7), we can see that the tangential component of $\boldsymbol{A}$ must be continuous, while its normal component may jump. In two-dimensional cases, this is not a problem since $\boldsymbol{A}$ will only have a component pointing outwards of the 2D plane. In the three-dimensional case, though, this jump in the normal component is problematic when using nodal finite elements to directly approximate $\boldsymbol{A}$, because all components are automatically continuous, which prohibits their use at interfaces between different materials. Additionally, the divergence of the current is violated at a jump of conductivity when the nodally interpolated vector potential is used [29]. One possibility is to introduce multiple nodes on the interface [30], but this causes problems when the interfaces are not flat [31]. Other methods involve a decomposition of the $H_0^{\Sigma}(curl, \Omega)$ space, but this can still lead to problems for jumps in permeability [32]. Since we expect both jumps in permeability and in conductivity between the different material regions in our induction heating applications, another element type should be used.

3.2 Edge Elements

To reformulate the previously discussed aspects on interface and boundary conditions in a mathematically consistent way, we can say that the finite elements must be conforming in $H(curl, \Omega)$. We use three-dimensional vectorial finite elements so the corresponding space of polynomials on Ω is a subspace of the space of infinitely often continuously differentiable functions $C^{\infty}(\Omega)^3$. Then, for any $\boldsymbol{u} \in C^{\infty}(\Omega)^3$, we can define an interpolate $\Pi \boldsymbol{u}$. The interpolates are denoted by $\Pi_1 \boldsymbol{u}$ on an element 1 and by $\Pi_2 \boldsymbol{u}$ on an element 2, where element 1 and element 2 share a common face F. Then we can state that a finite element is conforming in $H(curl)$ if and only if the tangential components of $\Pi_1 \boldsymbol{u}$ and $\Pi_2 \boldsymbol{u}$ are the same on F [33]. Without going deeper into the theoretical framework mainly developed by Nedelec [33], one can state that edge elements having their degrees of freedom on the edge of the element verify this condition. According to [7], the approximation of the vector potential $\boldsymbol{A}$ with edge finite elements of first kind can be written as

$$\boldsymbol{A} \approx \sum_{k=1}^{n_e} \boldsymbol{E}_k A_k, \tag{3.14}$$

where n_e is the total edge number and $\boldsymbol{E}_k$ the edge shape function of the k-th edge. The actual unknown A_k is defined as the integral of the magnetic vector potential along the edge k,

$$A_k = \int_k \boldsymbol{A} \cdot \mathrm{d}\boldsymbol{s}. \tag{3.15}$$

The edge shape function is constructed from the Lagrange shape functions of the nodes i and j constituting the edge k,

$$\boldsymbol{E}_k = (N_i \nabla N_j - N_j \nabla N_i) \,. \tag{3.16}$$

First order edge elements are divergence-free. However this does not mean that the computed fields are automatically divergent-free, since (surface) divergences may occur between two adjoining elements, as the normal component of the field may jump. Thus, some kind of gauging is still required if we are directly interested in the magnetic vector potential [31].

For obtaining the linear system from the weak form (3.13), we follow [7] and apply the same discretization used for $\boldsymbol{A}$ to the test function $\boldsymbol{A}'$, getting

$$\sum_{k=1}^{n_e}\sum_{l=1}^{n_e}\left(\int_\Omega \gamma \boldsymbol{E}_k \cdot \boldsymbol{E}_l \,\mathrm{d}\Omega \dot{A}_k + \int_\Omega \nu\left(\nabla\times\boldsymbol{E}_l\right)\cdot\left(\nabla\times\boldsymbol{E}_k\right) A_k \,\mathrm{d}\Omega - \int_\Omega \boldsymbol{E}_l\cdot\boldsymbol{J}_\mathrm{i}\,\mathrm{d}\Omega\right) = 0. \tag{3.17}$$

The linear system is given by

$$\boldsymbol{M}_A\dot{\boldsymbol{A}} + \boldsymbol{K}_A\boldsymbol{A} = \boldsymbol{f}, \tag{3.18}$$

where the time derivative can be discretized, using, e.g., the trapezoidal method. The harmonic case for an angular frequency ω can be written in the form of

$$\left(\boldsymbol{M}_A + \mathrm{j}\omega\boldsymbol{K}_A\right)\boldsymbol{A} = \boldsymbol{f}. \tag{3.19}$$

Evaluating the bilinear forms from (3.17) on an element Ω^e, leads to the following structure of the system matrices:

$$\boldsymbol{M}_A = [m_{pq}]\,; \quad m_{pq} = \int_{\Omega^e}\gamma\boldsymbol{E}_p\cdot\boldsymbol{E}_q\,\mathrm{d}\Omega, \tag{3.20}$$

$$\boldsymbol{K}_A = [k_{pq}]\,; \quad k_{pq} = \int_{\Omega^e}\nu\left(\boldsymbol{\mathcal{B}}_p^{curl}\right)^T\boldsymbol{\mathcal{B}}_q^{curl}\,\mathrm{d}\Omega, \tag{3.21}$$

$$\boldsymbol{f} = [f_p]\,; \quad f_p = \int_{\Omega^e}\boldsymbol{E}_p\cdot\boldsymbol{J}_\mathrm{i}\,\mathrm{d}\Omega. \tag{3.22}$$

The discretized curl operator $\boldsymbol{\mathcal{B}}_p^{curl}$ is given by

$$\boldsymbol{\mathcal{B}}_p^{curl} = \nabla\times\boldsymbol{E}_p. \tag{3.23}$$

Edge elements can lead to bad conditioning of the system matrices and cause decelerated convergence for some linear system solvers, e.g., those based on the conjugate gradient (CG) method [34]. Consequently, the linear solver must be chosen with great care to assure good numerical efficiency. One possibility to avoid this problem is to add a fictive conductivity γ' in the non-conducting domains [32].

3.3 Non-Conforming Interfaces

The skin effect is comparable to a boundary-layer problem. Thus, it is necessary to mesh the skin depth in the inductor and the sheet with a very fine mesh, while the surrounding air can be discretized in a coarser way. However, the use of conforming grids might lead to strongly distorted elements near the interfaces. Therefore it can be advantageous to use non-conforming interfaces, where conservation properties of the solution across the intersection interface are exploited.

The problem setup is shown in Fig. 3.1: the computational domain Ω is composed of two subdomains Ω_1 and Ω_2 with different discretizations and sharing the interface Γ_i. $\boldsymbol{n}$ is the common normal vector on Γ_I. The outer boundary $\partial\Omega$ can be split into a part where only Dirichlet BCs are imposed, denoted by Γ_e and a part with only Neumann BCs Γ_n. A first approach is the classical mortar method, described, e.g., in [35], which introduces a Lagrange multiplier g defined only on Γ_I and representing the flux of the solution across the boundary Γ_I. The continuity on the interface is enforced in a weak sense by defining the test function g' on the interface and adding an additional equation of the form

$$\int_{\Gamma_\mathrm{I}} g'\left(u_1 - u_2\right)\mathrm{d}\Gamma. \tag{3.24}$$

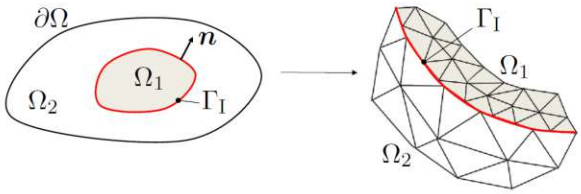

Figure 3.1: Non conforming interface between 2 computational regions Ω_1 and Ω_2 with different grids, image taken from [8].

This does not only have the disadvantage of adding a further unknown to the system, thus increasing the computational effort, but also the formulation of appropriate Lagrange multipliers for the magnetic vector potential is challenging.

A second technique used for non-conforming interfaces is the so-called Nitsche method, originally introduced in [36] to impose Dirichlet BCs in a weak sense. It has the advantage of not requiring any additional degrees of freedom (DOFs) and leading to symmetric system matrices. From this point on, we adopt the approach from [8], as this corresponds to the implementation of non-conforming interfaces for edge elements in openCFS. However, the following derivation is application-oriented. Further details regarding the mathematical background, such as indications on function spaces and error measures, can be found in [8].

To start with, we define jump- and average operators across the common facet F of 2 elements T_1 and T_2 belonging to Ω_1 and Ω_2 respectively. The jump operator for an arbitrary vector valued quantity $\boldsymbol{u}$ is redefined on element level as

$$[\boldsymbol{u}] = \begin{cases} \boldsymbol{u}|_{T_1} - \boldsymbol{u}|_{T_2}, & \text{if} \quad F \not\subset \partial\Omega \\ \boldsymbol{u}|_T, & \text{if} \quad F \subset \partial\Omega. \end{cases} \tag{3.25}$$

Equally, the average operator is defined as

$$\{\boldsymbol{u}\}_\nu = \begin{cases} \bar{\nu}_1 \boldsymbol{u}|_{T_1} + \bar{\nu}_2 \boldsymbol{u}|_{T_2}, & \text{if} \quad F \not\subset \partial\Omega \\ \boldsymbol{u}|_T, & \text{if} \quad F \subset \partial\Omega, \end{cases} \tag{3.26}$$

with the coefficients

$$\bar{\nu}_1 = \frac{\nu_1}{\nu_1 + \nu_2} \quad \text{and} \quad \bar{\nu}_2 = \frac{\nu_2}{\nu_1 + \nu_2}. \tag{3.27}$$

The basic idea is to impose the continuity conditions (3.6) and (3.7) by adding additional integral terms, thus enforcing the continuity of the unknown in a weak sense. Starting from (3.13), we neglect Dirichlet BCs, such that the last term on the right-hand side only contains entries for the non-conforming interface. Taking into account (3.7) $\nu_1 \nabla \times \boldsymbol{A_1} \times \boldsymbol{n} = \nu_2 \nabla \times \boldsymbol{A_2} \times \boldsymbol{n}$, the boundary term on a common facet F can be rewritten as

$$-\int_F \{\nabla \times \boldsymbol{A} \times \boldsymbol{n}\}_\nu \cdot [\boldsymbol{A}'] \,. \tag{3.28}$$

We then add a similar term, switching unknown and test function to symmetrize the system

$$-\int_F \{\nabla \times \boldsymbol{A}' \times \boldsymbol{n}\}_\nu \cdot [\boldsymbol{A}] \,. \tag{3.29}$$

Finally, the so-called penalty term defined by the Nitsche parameter β is added to assure the condition (3.6) $\boldsymbol{n} \times \boldsymbol{A}_1 = \boldsymbol{n} \times \boldsymbol{A}_2$

$$\beta \int_F \frac{\bar{\nu} p_{\mathrm{E}}^2}{h_{\mathrm{E}}} [n \times \boldsymbol{A}] \cdot [n \times \boldsymbol{A}'], \tag{3.30}$$

where h_{E} denotes a characteristic element length scale and p_{E} the element order. In the absence of Dirichlet boundary conditions, the above defined surface terms only have contributions on the non-conforming interface. Denoting by $\mathcal{F}_h^I$ the set of faces on the interface Γ_{I}, the total weak form (3.13) can be rewritten as

$$\begin{aligned} &\int_\Omega \nabla \times \boldsymbol{A}' \cdot \nu \nabla \times \boldsymbol{A} + \kappa \int_\Omega \gamma \boldsymbol{A}' \cdot \boldsymbol{A} - \sum_{F \in \mathcal{F}_h^I} \int_F \{\nabla \times \boldsymbol{A} \times \boldsymbol{n}\}_\nu \cdot [\boldsymbol{A}'] - \\ &\sum_{F \in \mathcal{F}_h^I} \int_F \{\nabla \times \boldsymbol{A}' \times \boldsymbol{n}\}_\nu \cdot [\boldsymbol{A}] + \sum_{F \in \mathcal{F}_h^I} \beta \int_F \frac{\bar{\nu} p_{\mathrm{E}}^2}{h_{\mathrm{E}}} [n \times \boldsymbol{A}] \cdot [n \times \boldsymbol{A}'] = \int_\Omega \boldsymbol{A}' \cdot \boldsymbol{J}_{\mathrm{i}}. \end{aligned} \tag{3.31}$$

κ indicates the analysis type (static, harmonic transient) $\kappa \in \{0, \gamma\partial/\partial t, \mathrm{j}\omega\gamma\}$, so the formulation is valid for all analysis types.

The fully discretized linear system takes the form

$$\begin{bmatrix} \boldsymbol{K}_{11} & \boldsymbol{0} \\ \boldsymbol{0} & \boldsymbol{K}_{22} \end{bmatrix} \begin{bmatrix} \boldsymbol{u}_1 \\ \boldsymbol{u}_2 \end{bmatrix} + \kappa \begin{bmatrix} \boldsymbol{M}_{11} & \boldsymbol{0} \\ \boldsymbol{0} & \boldsymbol{M}_{22} \end{bmatrix} \begin{bmatrix} \boldsymbol{u}_1 \\ \boldsymbol{u}_2 \end{bmatrix} + \begin{bmatrix} \boldsymbol{K}_{\Gamma_1} & \boldsymbol{K}_{\Gamma_1\Gamma_2} \\ \boldsymbol{K}_{\Gamma_2\Gamma_1} & \boldsymbol{K}_{\Gamma_2} \end{bmatrix} \begin{bmatrix} \boldsymbol{u}_1 \\ \boldsymbol{u}_2 \end{bmatrix} = \begin{bmatrix} \boldsymbol{f}_1 \\ \boldsymbol{f}_2 \end{bmatrix}. \tag{3.32}$$

Note that the stiffness matrices $\boldsymbol{K}_{11}$ and $\boldsymbol{K}_{22}$, as well as the mass matrices $\boldsymbol{M}_{11}$ and $\boldsymbol{M}_{22}$ are computed separately on the 2 subdomains Ω_1 and Ω_2. Given that $\boldsymbol{K}_{\Gamma_2\Gamma_1} = (\boldsymbol{K}_{\Gamma_1\Gamma_2})^T$, the linear system is symmetric.

The coupling matrices have to be evaluated on an intersection grid, which is composed of lines in the 2D case and surfaces in the 3D case. For straight interfaces, the intersection can be computed from comparing the ranges of all coordinates of elements on the interface. For structured 3D hexaedral elements, the computation is also straight-forward since for axiparallel surface grids, the intersection of two elements will also be an axiparallel quadrilateral. For curved interfaces, the procedure is more complicated, since the elements are possibly not coplanar and projections are required [37]. In any case the intersection grid just determines the position of the integration points, the shape functions are still evaluated on the respective interface sides Γ_1 and Γ_2 [8].

3.4 Inductor Excitation

In the numerical simulation of induction heating setups, the power input comes from prescribing a certain current or voltage at the ports of the inductor. A very simple approach to model the excitation current in the case of negligible skin effect is the loading with a constant current density [7]. The setup is shown in Fig. 3.2(a) and is only valid for thin wires and a high filling factor (dense arrangement of the wires). In that case, the coil consisting of several wires can be reduced to a cylinder. The total current density can be computed from

$$\boldsymbol{J}_{\mathrm{i}} = \frac{IN}{\kappa \Gamma_c} \boldsymbol{e}_{\mathrm{J}}, \tag{3.33}$$

where I is the total current through the coil, N the number of turns, κ the filling factor and Γ_c the cross section of the hollow cylinder. This expression can directly be inserted into the right-hand-side of the weak formulation of the curl-curl problem (3.13). In simulation, the conductivity of the coil region is set to zero, since we assume that the individual wires are isolated from each other and we do not compute eddy currents in that region.

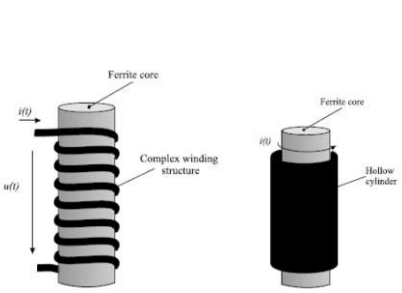

(a) Current density excitation, image taken from [7].

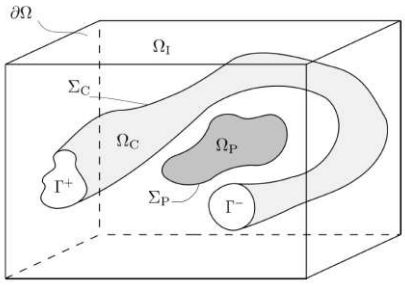

(b) Domain definition, image taken from [8].

Figure 3.2: Different inductor excitation modes.

For efficiency computations, this approach is not applicable because it does not allow the computation of the frequency dependent resistance of the inductor. It is possible to consider the skin-effect in the conductor region even in the temporally gauged formulation of the eddy current problem, where the electric scalar potential is set to $V = 0$. The total current can be split into an impressed and an eddy current part, but this is computationally very inefficient, because the DOFs of the inductor will be coupled to all other DOFs of the other regions [8]. Furthermore, the numerical stability is rather inferior [38].

Thus, we need to consider formulations of the eddy current problem without the temporal gauge. The following derivations regarding the so-called $A - V, A$ formulation are all taken from [8]. With the definition of the scalar electric potential (2.12), the ungauged strong form of the eddy current problem is obtained as

$$\nabla \times \nu \nabla \times \boldsymbol{A} + \gamma \frac{\partial \boldsymbol{A}}{\partial t} + \gamma \nabla V = \boldsymbol{J}_{\mathrm{i}}. \tag{3.34}$$

V is non-zero only in conducting regions. Since we have an additional unknown, we also need a second equation. The divergence-free property of the total current density

$$-\nabla \cdot \left(\gamma \nabla V + \gamma \frac{\partial \boldsymbol{A}}{\partial t} \right) = 0, \tag{3.35}$$

can be used. Before deriving the respective weak forms, we take a closer look at the computational domain, shown in Fig. 3.2(b). The domain Ω is divided into 3 subdomains: an inductor domain Ω_{C}, a non-conducting domain Ω_{I} (air) and a conducting domain Ω_{P} where eddy currents are induced. The outer boundary is denoted by $\partial\Omega$ and the conductor region Ω_{C} shares only the electric ports Γ^+ and Γ^- with $\partial\Omega$. The magnetic boundary and interface conditions for (3.34) are the same as in the previous points, but we also have the electric BC $\boldsymbol{n} \times \boldsymbol{E} = \boldsymbol{0}$ on $\partial\Omega$. Using (2.12), this can be rewritten as

$$\boldsymbol{n} \times \boldsymbol{E} = \boldsymbol{n} \times \left(-\nabla V - \frac{\partial \boldsymbol{A}}{\partial t} \right) = 0 \quad \text{on} \quad \partial\Omega. \tag{3.36}$$

This is equivalent to setting the two terms to zero individually. The second term $\frac{\partial \boldsymbol{A}}{\partial t}$ is always zero on $\partial\Omega$ when using edge elements. The first condition $\nabla V = 0$ is equivalent to a constant electric scalar potential

$$V = V_0 = const \quad \text{on} \quad \partial\Omega. \tag{3.37}$$

As a consequence, the weak forms of (3.34) and (3.35) can be formulated as: Find $\boldsymbol{A} \in H_0(curl, \Omega)$ and $V \in \tilde{W} = \{w \in H^1(\Omega) | w|_{\Gamma^+} = V_+, w|_{\Gamma^-} = V_-\}$ such that

$$\int_\Omega \nabla \times \boldsymbol{A} \cdot \nu \nabla \times \boldsymbol{A}' \,\mathrm{d}\Omega + \int_{\Omega_{\mathrm{C,P}}} \gamma \frac{\partial \boldsymbol{A}}{\partial t} \cdot \boldsymbol{A}' \,\mathrm{d}\Omega + \int_{\Omega_\mathrm{C}} \gamma \nabla V \cdot \boldsymbol{A}' \,\mathrm{d}\Omega = \int_{\Omega_\mathrm{C}} \boldsymbol{J}_\mathrm{i} \cdot \boldsymbol{A}' \,\mathrm{d}\Omega \tag{3.38}$$

$$- \int_{\Omega_\mathrm{C}} \gamma \frac{\partial \boldsymbol{A}}{\partial t} \cdot \nabla V' \,\mathrm{d}\Omega - \int_{\Omega_\mathrm{C}} \gamma \nabla V \cdot \nabla V' \,\mathrm{d}\Omega = 0 \tag{3.39}$$

$$\forall \boldsymbol{A}' \in H_0(curl, \Omega), \forall V' \in H_0^1(\Omega)$$

It can be shown that fixing the Dirichlet values of V with a voltage $U(t)$, e.g., by prescribing

$$V|_{\Gamma^+} = U(t) \qquad\qquad V|_{\Gamma^+} = 0, \tag{3.40}$$

matches the definition of voltage based on power $P = U(t)I(t)$ [12].

To make the computation of field values in the inductor more efficient, a modified $A-V, A$ formulation is developed in [8]. It is based on the fact that the electric field strength on Ω_C does not depend on the values of V on $\Omega_\mathrm{C}/\{\Gamma^+ \cup \Gamma^-\}$ if the boundary conditions $V_{\Gamma^+} = U(t)$ and $V_{\Gamma^+} = 0$ are fulfilled and $V \in H^1(\Omega)$ [12].

The obvious way of determining a solution for V verifying the conditions stated above is solving the electric flow problem given in its weak form by: Find $\tilde{V} \in H^1(\Omega)$ such that

$$\int_{\Omega_\mathrm{C}} \gamma \nabla \tilde{V} \cdot \nabla \tilde{V}' \,\mathrm{d}\Omega = 0, \qquad \forall \tilde{V}' \in H_0^1(\Omega). \tag{3.41}$$

Considering that this PDE is linear, it is possible to use the voltage $U(t)$ as a multiplication factor for the solution of (3.41) with unit boundary conditions $V_{0\Gamma^+} = 1$ and $V_{0\Gamma^+} = 0$, redefining $\tilde{V}$ as $\tilde{V} = U(t)\tilde{V}_0$.

For voltage excitation, one can now simply replace V with the precomputed $\tilde{V}_0$ in (3.38) on Ω_C. The divergence of the total current density in the conductor is

$$\nabla \cdot \boldsymbol{J} = -\nabla \cdot \left(\gamma U(t) \nabla \tilde{V}_0 + \gamma \frac{\partial \boldsymbol{A}}{\partial t} \right). \tag{3.42}$$

For a prescribed voltage $U(t)$ it is zero, since the term containing $\boldsymbol{A}$ is zero when using edge elements and the second term is zero through (3.41).

An excitation with a total current I is only possible in a weak sense by using the weak form of the total current density as an additional constraint:

$$\int_{\Omega_\mathrm{C}} \gamma \frac{\partial \boldsymbol{A}}{\partial t} \cdot \nabla \tilde{V}_0' \,\mathrm{d}\Omega + U(t) \int_{\Omega_\mathrm{C}} \gamma \nabla \tilde{V}_0 \cdot \nabla \tilde{V}_0' \,\mathrm{d}\Omega = I. \tag{3.43}$$

3.5 Heat Coupling

The Joule losses due to the resistance of the sheet are volumetric heat sources $\dot{q}_v$ for the heat problem derived in Sec. 2.3. Neglecting hysteresis losses, the instantaneous Joule losses are given by the relation

$$\dot{q}_v = \boldsymbol{J} \cdot \boldsymbol{E}. \tag{3.44}$$

Since we do not have any impressed current density $\boldsymbol{J}_\mathrm{i}$ in the sheet, we can use (2.5) to express the Joule losses as

$$\dot{q}_v = \gamma \boldsymbol{E} \cdot \boldsymbol{E}. \tag{3.45}$$

As already stated when defining the eddy current problem, we neglect the velocity of the sheet for the electromagnetic problem and only take it into account through the convective term in the heat equation, since in the sheet velocity range for our applications this term is dominant. Finally, using the definition of $\boldsymbol{E}$ through the magnetic vector potential, we can rewrite the instantaneous Joule losses (in a gauged formulation) as

$$\dot{q}_v = \gamma \frac{\partial \boldsymbol{A}}{\partial t} \cdot \frac{\partial \boldsymbol{A}}{\partial t}. \tag{3.46}$$

To realize this coupling in an efficient way, we presume that the time scale for the eddy current problem is notably smaller than the characteristic heat diffusion time scale, so we average the Joule losses over an eddy current time cycle [19]. As a matter of fact, the excitation frequency according to Sec. 2.5 is in the range of 1-100 kHz, while the empirical time constant for the heating of steel sheets is in the order of magnitude of $1 \cdot 10^{-1}$s [8].

To take the period average from (3.46), integration over one period T is necessary

$$\bar{q}_v = \frac{1}{T} \int_0^T \gamma \frac{\partial \boldsymbol{A}}{\partial t} \cdot \frac{\partial \boldsymbol{A}}{\partial t} \, \mathrm{d}t. \tag{3.47}$$

We have a harmonic excitation with the excitation frequency ω and a period $T = \frac{2\pi}{\omega}$. Only the real part of (3.46) contributes to the Joule losses. Hence, using the complex amplitude $\hat{\boldsymbol{A}}$ and its conjugate complex $\hat{\boldsymbol{A}}^*$, the integral can be rewritten as

$$\bar{q}_v = \frac{\omega}{2\pi} \gamma \omega^2 \int_0^{\frac{2\pi}{\omega}} \left[\frac{1}{2} \left(\hat{\boldsymbol{A}} e^{j\omega t} + \hat{\boldsymbol{A}}^* e^{-j\omega t} \right) \right]^2 \mathrm{d}t. \tag{3.48}$$

Since we are integrating over one period, the terms with $e^{2j\omega t}$ and $e^{-2j\omega t}$ vanish and the simplified form of the period averaged Joule losses is given by

$$\bar{q}_v = \frac{1}{2} \gamma \omega^2 \hat{\boldsymbol{A}} \cdot \hat{\boldsymbol{A}}^* = \frac{1}{2} \gamma \omega^2 |\hat{\boldsymbol{A}}|^2. \tag{3.49}$$

The weak form for the thermal problem is obtained from (2.34), assuming a static regime and using the time averaged Joule losses $\bar{q}_v$ as volumetric heat sources [19]. It states: Find the temperature ϑ such that

$$\int_\Omega \nabla \vartheta' \cdot (\lambda \nabla \vartheta) \, \mathrm{d}\Omega + \int_\Omega \vartheta' \rho c_p \boldsymbol{v} \cdot \nabla \vartheta \, \mathrm{d}\Omega - \int_\Gamma \vartheta' \nabla \vartheta \cdot \boldsymbol{n} \, \mathrm{d}\Gamma = \int_\Omega \vartheta' \bar{q}_v \, \mathrm{d}\Omega, \tag{3.50}$$

for all test functions ϑ'. The boundary term $\int_\Gamma \vartheta' \nabla \vartheta \cdot \boldsymbol{n} \, \mathrm{d}\Gamma$ is evaluated depending on the boundary conditions discussed in Sec. 2.3.

Chapter 4

Analytical Solution Approaches

Preceding the advent of numerical simulation tools, a great variety of analytical design methods for induction heating appliances were developed [39]. Unfortunately, they mostly exploit the rotational symmetry of the setup, e.g., for induction furnaces [40]. To obtain quantitatively accurate results for the case of (thin) metal sheets, one has to rely on numerical methods. Still, an attempt will be made to present some analytical solutions that can be helpful in understanding the dependency of the efficiency on the frequency and various system parameters.

4.1 Preliminary Considerations on Efficiency

At first, we need to reconsider the notion of electrical efficiency (2.37) to gain a more intuitive understanding of the dependencies that can be useful to interpret simulation results. The schematic induction heating setup in Fig. 4.1 can be considered as a transformer analogy, defining the inductor as primary coil and the sheet as closed secondary circuit [22]. However, inside the coil the total magnetic flux Φ divides into one air gap component Φ_{gap} and one component within the sheet Φ_{sheet} that induces a voltage in the sheet and produces the desired heating through Joule losses. Since Φ_{gap} represents an important part of the total flux and results in purely reactive power, the power factor of induction heating setups is always low, in some cases even smaller than 0.1 [41]. Moreover, a significant part of the magnetomotive force NI of the inductor is delivered outside of the coil in the return flux path.

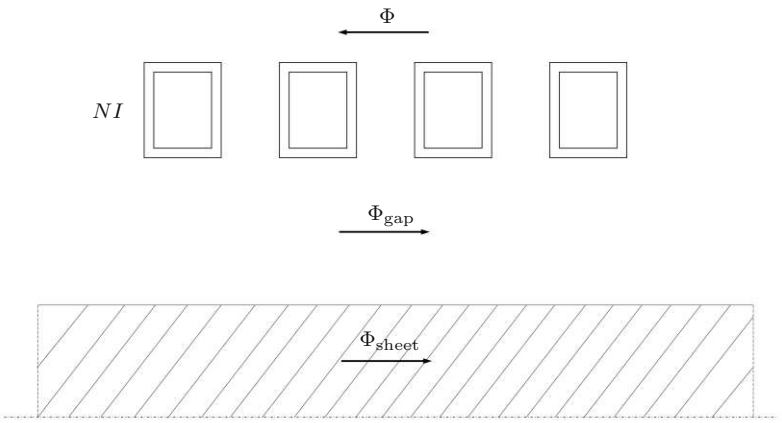

Figure 4.1: Inductor-sheet system for N coils and an excitation current I, image adapted from [1].

This effect is particularly pronounced for the "short" coils used in LFH and TFH setups. For cylindrical workpieces, there are formulas for the computation of the equivalent magnetic reluctances for the air gap and return path derived from the reluctance of an empty coil of infinite axial length [40]. For LFH and TFH setups, the field line distribution around the inductor is not rotationally symmetric, so we need to find a different approach.

Neglecting stray and return path losses, the efficiency can be reformulated as

$$\eta = \frac{R_{\text{sheet}}}{R_{\text{sheet}} + R_{\text{ind}}}, \tag{4.1}$$

where R_{sheet} is the resistance associated with the Joule losses in the sheet, while R_{ind} describes the resistive losses in the inductor. While this chapter is mainly concerned with the description of the sheet resistance R_{sheet}, a few aspects regarding the resistance of the inductor should not be left unmentioned. In the context of this thesis, hollow water-cooled conductors of rectangular cross-section are used. Evidently, the resistance in the inductor will also depend on the skin effect so that for high frequencies the AC resistance depends on the perimeter of the inductor cross section rather than on its area. Approximate formulas describing this effect have been known for some time and have been successfully employed in various applications, such as white-box modelling of power transformers of arbitrary cross-sections [42]. For thin rectangular conductors, where the height is much larger than the width, these formulas work well and even a one-dimensional analytical solution can be derived [43]. However, for aspect ratios close to 1, as in our case, the two-dimensional edge effects have to be taken into account and an analytical solution is challenging to find, mainly due to the difficulty of stating consistent BCs [44]. Commonly used solutions are correction factors for the one-dimensional case [45] or empirical formulas derived from extensive FEM parameter studies [46]. These approaches are either cumbersome to use or have a restricted validity range, so for a qualitative understanding, we will just assume an inverse dependency on the skin depth in the inductor, namely $R_{\text{sheet}} \sim 1/\delta$ [15] [47].

4.2 Plates of Finite Thickness

In Sec. 2.2, the diffusion equation describing the propagation of the electromagnetic field quantities for the infinite half-plane was solved to illustrate the skin effect and introduce the notion of skin depth. For the heating of metal sheets one needs to take into account the finite thickness of the heated objects. We need to reconsider the solution found in (2.26) under the angle that we now also have an air region below the plate, following [48]. In the first place, we assume a homogeneous field intensity at the top surface of a plate of finite thickness, corresponding to unilateral heating. As already discussed, the induced sheet currents are the inverse image of the inductor currents and will have significant values only below the inductor. Hence, to get an approximate expression for the frequency dependency of the induced Joule losses, the system can be reduced to considering the effect of two infinitely long conductors placed above and below the sheet and directed along the x-axis [24]. In this simplified situation, LFH and TFH heating principles differ only by the direction of the conductor currents and can be obtained from the unilateral case using superposition according to Fig. 4.2. For LFH, the inductor currents above and below the sheet are oriented in opposite directions, leading to a magnetic field in the same direction on both sides of the sheet. For TFH, the currents are oriented in the same direction and the magnetic field is oriented in the opposite direction on the two sides of the sheet. Again, only harmonic excitations are considered. To simplify the notation, we denote the amplitude $\hat{H}_y$ simply by H_y.

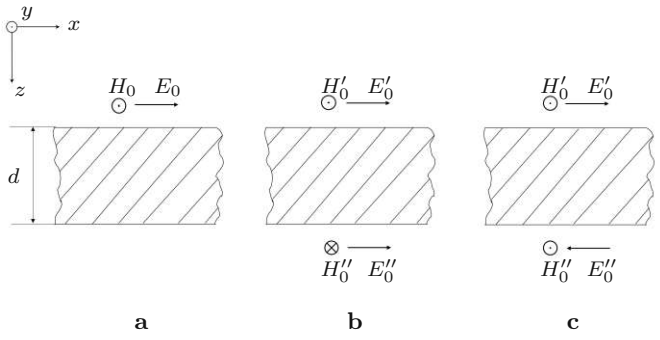

Figure 4.2: Different current configurations: **a** unilateral heating, **b** bilateral heating with currents in the same direction, **c** bilateral heating with currents in the opposite direction, image adapted from [48].

In the plate region, where the eddy currents are induced, (2.22) still holds

$$\frac{\partial^2 H_y}{\partial z^2} = k^2 H_y. \tag{4.2}$$

Neglecting the displacement current density in the non-conducting air region below the plate we find for this region (denoted by index 1)

$$\frac{\partial^2 H_{1y}}{\partial z^2} = 0. \tag{4.3}$$

In the sheet we need to account for reflected waves, so the complete ansatz for the magnetic field intensity has to be used in (4.2)

$$H_y(z) = C_1 e^{kz} + C_2 e^{-kz}. \tag{4.4}$$

For the air region below the plate, it is sufficient to use the ansatz

$$H_{1y}(z) = C_3 e^{-k_1 z}, \tag{4.5}$$

since no reflected waves will appear in this case. Inserting this ansatz in (4.3), it trivially follows that $C_3 = 0$ and $H_{1y} = 0$. Using the boundary condition $H_y(z = 0) = H_0$ as well as the continuity of the tangential component of H at the bottom of the plate $H_y(z = d) = 0$, one obtains the equations for the integration constants

$$C_1 + C_2 = H_0, \tag{4.6}$$

$$C_1 e^{-kd} + C_2 e^{kd} = 0. \tag{4.7}$$

Based on this, the field intensity inside the plate can be written as

$$H_y = H_0 \frac{e^{-kz} - e^{-2kd} e^{kx}}{1 - e^{-2kd}}. \tag{4.8}$$

Replacing the exponential functions with hyperbolic ones, this simplifies to

$$H_y = H_0 \frac{\sinh\left[k(d - z)\right]}{\sinh(kd)}. \tag{4.9}$$

From Maxwell's law, we can easily obtain the electric field intensity, namely

$$\boldsymbol{E} = \frac{1}{\gamma} \nabla \times \boldsymbol{H}, \tag{4.10}$$

which in our case reduces to

$$E_x = -\frac{1}{\gamma} \frac{\partial H_y}{\partial z}. \tag{4.11}$$

Using the expression found in (4.9), the electric field intensity is given by

$$E_x = H_0 \frac{k}{\gamma} \frac{\cosh\left[k(d-z)\right]}{\sinh(kd)}. \tag{4.12}$$

Based on these relations, we can derive the fields for the case of bilateral heating, depicted in Fig. 4.2. In the case of currents in the same direction, as encountered in TFH, the electric field intensities E_0' and E_0'' have equal amplitude and phase, while the magnetic field intensities H_0' and H_0'' are opposed. Inside the plate, the currents will also flow in the same direction. Thus, at an arbitrary point at a distance z from the sheet surface, there will be superposition of the electromagnetic field intensities E' and E'' as well as H' and H''

$$H_y = H_y' - H_y'', \tag{4.13}$$

$$E_x = E_x' + E_x''. \tag{4.14}$$

To account for symmetry, $H_y' = H_y''$ in the middle of the plate, such that we have $H_y(z = d/2) = 0$. Based on (4.9), the individual components H' and H'' can be written as

$$H_y' = H_0 \frac{\sinh\left[k(d-z)\right]}{\sinh(kd)}, \tag{4.15}$$

$$H_y'' = H_0 \frac{\sinh\left(kz\right)}{\sinh(kd)}. \tag{4.16}$$

This can be inserted into (4.13) and after some mathematical transformations, one finds

$$H_y' = H_0 \frac{\sinh\left[k\left(\frac{d}{2} - z\right)\right]}{\sinh\left(k\frac{d}{2}\right)}. \tag{4.17}$$

For induction heating, we are mainly interested in the current density distribution $J_x(z)$ in the plate, which when using (4.11) and $J_x = \gamma E_x$ is given by

$$J_x = H_0 k \frac{\cosh\left[k\left(\frac{d}{2} - z\right)\right]}{\sinh\left(k\frac{d}{2}\right)}. \tag{4.18}$$

In order to get results for practical applications, we have to compute the norm of the complex functions derived above. For the current density this yields

$$\frac{|J|}{|J_0|} = \sqrt{\frac{\cosh\left(\frac{d-2z}{\delta}\right) + \cos\left(\frac{d-2z}{\delta}\right)}{\cosh\left(\frac{d}{\delta}\right) - \cos\left(\frac{d}{\delta}\right)}}, \tag{4.19}$$

where the eddy current density $|J_0|$ on the surface is given by $|J_0| = \frac{\sqrt{2}H_0}{\delta}$ and δ again denotes the skin penetration depth defined in (2.25). The resulting Joule loss power densities can be computed from

$$p = \frac{1}{2\gamma} J^2. \tag{4.20}$$

The total heating power P in the plate can be obtained by plugging (4.19) into (4.20) and integrating over the sheet thickness d

$$\begin{aligned} P &= \int_0^d p \, \mathrm{d}z \\ &= \frac{1}{\gamma} \left(\frac{H_0}{\delta} \right)^2 \int_0^d \frac{\cosh\left(\frac{d-2z}{\delta}\right) + \cos\left(\frac{d-2z}{\delta}\right)}{\cosh\left(\frac{d}{\delta}\right) + \cos\left(\frac{d}{\delta}\right)} \, \mathrm{d}z \\ &= \frac{H_0^2}{2\delta\gamma} \frac{\sinh\left(\frac{d}{\delta}\right) + \sin\left(\frac{d}{\delta}\right)}{\cosh\left(\frac{d}{\delta}\right) - \cos\left(\frac{d}{\delta}\right)}. \end{aligned} \tag{4.21}$$

For the case of opposite currents, corresponding to the LFH case, the electric field intensities E_0' and E_0'' have opposite directions, while the magnetic field intensities H_0' and H_0'' are equal in amplitude and phase and the resulting field quantities can be written as

$$H_y = H_y' + H_y'', \tag{4.22}$$

$$E_x = E_x' - E_x''. \tag{4.23}$$

Using the same approach as before, the resulting absolute value of the current density can be found as

$$\frac{|J|}{|J_0|} = \sqrt{\frac{\cosh\left(\frac{d-2z}{\delta}\right) - \cos\left(\frac{d-2z}{\delta}\right)}{\cosh\left(\frac{d}{\delta}\right) - \cos\left(\frac{d}{\delta}\right)}}. \tag{4.24}$$

The total heating power is given by

$$P = \frac{H_0^2}{2\delta\gamma} \frac{\sinh\left(\frac{d}{\delta}\right) - \sin\left(\frac{d}{\delta}\right)}{\cosh\left(\frac{d}{\delta}\right) + \cos\left(\frac{d}{\delta}\right)}. \tag{4.25}$$

Comparing (4.21) and (4.25), one can see that they only differ by the second factor depending on the ratio d/δ, which can be denoted by λ_{TFH} and λ_{LFH} respectively

$$\lambda_{\mathrm{TFH}} = \frac{\sinh\left(\frac{d}{\delta}\right) + \sin\left(\frac{d}{\delta}\right)}{\cosh\left(\frac{d}{\delta}\right) - \cos\left(\frac{d}{\delta}\right)}, \tag{4.26}$$

$$\lambda_{\mathrm{LFH}} = \frac{\sinh\left(\frac{d}{\delta}\right) - \sin\left(\frac{d}{\delta}\right)}{\cosh\left(\frac{d}{\delta}\right) + \cos\left(\frac{d}{\delta}\right)}. \tag{4.27}$$

Comparing the eddy current distributions over the plate thickness in Fig. 4.3, one can see that for TFH, the current distribution is practically constant for ratios of d/δ below one, while for LFH, the distribution is very uneven, with vanishing currents in the middle of the plate. The zero current density in the plate centre results from enforcing symmetry in (4.23). When a homogeneous heating of the plate over thickness direction is required, it can be of advantage to use TFH.

Regarding the optimal frequency, the curve of the characteristic coefficients λ_{LFH} and λ_{TFH} in Fig. 4.2 gives some qualitative insights. For LFH, λ_{LFH} is maximal at a ratio of $d/\delta = 2.7$ approximately, while for a further increase of the d/δ ratio, the coefficient goes to 1. An estimate of the optimal frequency can be obtained from this relation. For TFH, one can only see that the λ_{TFH} value decreases with increasing ratios d/δ, asymptotically approaching the value of 1 as well. Theoretically λ_{TFH} would go to infinity for d/δ approaching zero, but this is not physical. Hence, we cannot deduce any optimal d/δ ratio. Furthermore, in TFH (at least for lower frequencies) we have a vertical component of the magnetic field passing through the plate. This cannot be modelled with the chosen approach, such that the solutions derived in this section can only give approximate qualitative relations for the TFH case.

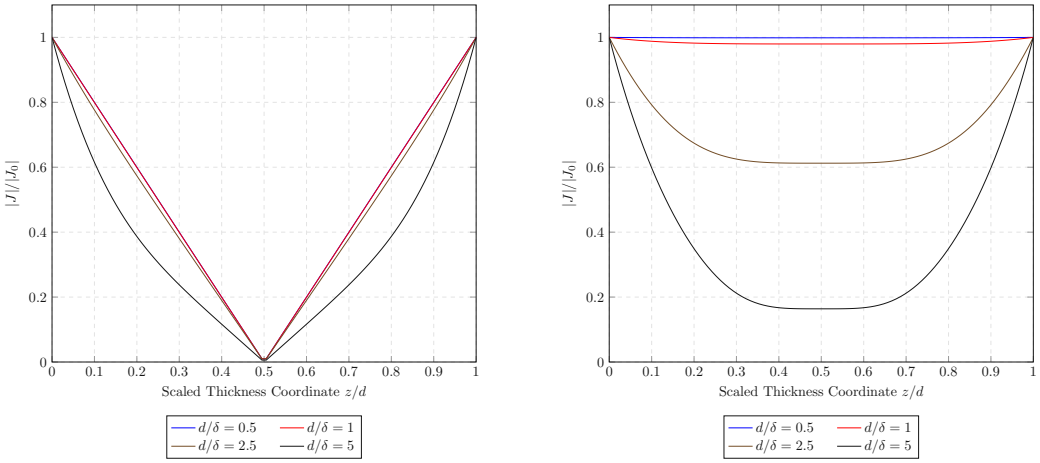

(a) Opposite currents (LFH)

(b) Currents in same direction (TFH)

Figure 4.3: Analytical eddy current density scaled by maximum eddy current density over dimensionless sheet thickness coordinate.

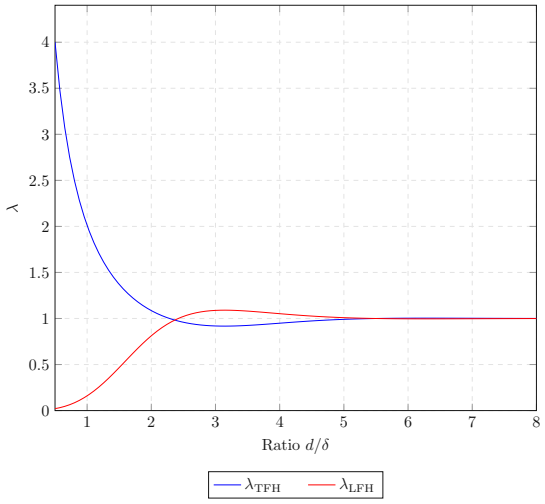

Figure 4.4: Comparison of the characteristic coefficients λ_{LFH} and λ_{TFH} over different ratios of d/δ.

Still, the indicated empirical ranges of the d/δ ratios introduced in Sec. 2.5 can be justified by the comparison of λ_{LFH} and λ_{TFH}.

4.3 Straight Current Filament over Plate of Infinite Thickness

In the cases considered previously, the magnetic field distribution at the surface was a known quantity and we only derived its propagation into the plate. In induction heating setups, though, the magnetic field quantities at the plate surface are not known a priori and have to be determined based on the arrangement of the conductors. Analytical solutions are available for the case of a straight current filament parallel to the plate. In theory, results ca be obtained for arbitrary conductor configurations, using the superposition principle. Another advantage of this approach is that stray and return path losses will be automatically taken into account by this solution, since the distribution of the magnetic field around the conductor is evaluated.

We assume a plate of infinite thickness, a simplification that will be justified later through comparison to numerical results, obtained with the computational model from Fig. 4.5(b). The derivation follows [13] and [49]. This time we are also interested in the field variation above the plate, so the coordinate system is rotated as compared to the previous layouts, as shown in Fig. 4.5(a). The field values change not only in the direction of the plate thickness, but also in the x direction parallel to the plate surface. Thus, the separation of variables method has to be used and it is favourable to use the magnetic vector potential $\boldsymbol{A}$, as $\boldsymbol{A}$ has a single component in z-direction.

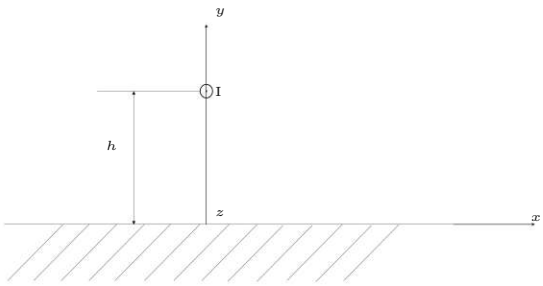

(a) Filament carrying a current I at a distance h from a plate of infinite thickness, image adapted from [49].

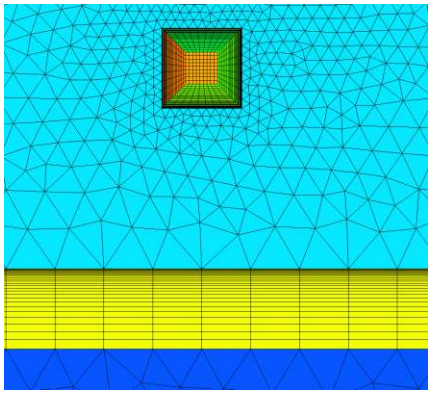

(b) Computational model with conductor of width b_{ind} and sheet thickness d. Orange inner inductor part is water. Sheet in yellow.

Figure 4.5: Models for a current filament over a plate.

Denoting by 1 the air region above the plate and by 2 the conducting plate region, the diffusion equations for the magnetic vector potential are obtained by

$$\nabla^2 A_{1z} = 0, \tag{4.28}$$

$$\nabla^2 A_{2z} = k^2 A_{2z} = \mathrm{j}p^2 A_{2z}, \tag{4.29}$$

with $p^2 = \omega\mu\gamma$. The solution for $\boldsymbol{A}$ must be symmetric with respect to the y-axis. In the air region 1, there is a superposition of the fields from the current filament and the induced eddy currents in the plate. In the plate region 2, $y < 0$ and the solution has to vanish for $y \to -\infty$. The following ansatz formulations for the magnetic vector potential fulfill the physical behaviour described above

$$A_1(x,y) = \int_0^\infty \left(C_1 e^{my} + C_2 e^{-my}\right) \cos(mx)\,\mathrm{d}m, \tag{4.30}$$

$$A_2(x,y) = \int_0^\infty C_3 e^{qmy} \cos(mx)\,\mathrm{d}m. \tag{4.31}$$

Here, m (with dimension 1/m) is the constant of the separation of variables, while q is an additional variable for the sheet region defined by $q = \sqrt{m^2 + \mathrm{j}p^2}$.

The components of the magnetic flux density can obtained by

$$B_x = \frac{\partial A}{\partial y}, \tag{4.32}$$

$$B_y = -\frac{\partial A}{\partial x}. \tag{4.33}$$

Taking into account the sign convention for y, the term e^{my} in (4.30) describes the field due to the current filament. Consequently, Ampere's law for the current filament can be used to determine C_1, namely

$$B_1(x,y) = \frac{\mu_0 I}{2\pi r}, \tag{4.34}$$

with $r = \sqrt{x^2 + (b-y)^2}$ as the distance from the filament. For the region between the filament and the plate, the condition (4.34) can be evaluated using (4.32) and (4.33) to give

$$C_1 = \frac{\mu_0 I}{2\pi} \frac{e^{-hm}}{m}. \tag{4.35}$$

To determine C_2 and C_3, the interface conditions described in Sec. 2.1 have to be used

$$B_{1y} = B_{2y}, \tag{4.36}$$

$$\frac{1}{\mu_0} B_{1x} = \frac{1}{\mu} B_{2x}. \tag{4.37}$$

Defining the relative permeability $\mu_r = \mu_2/\mu_0$, the integration constants can be obtained as

$$C_2 = \frac{\mu_0 I}{2\pi} \frac{\mu_r m - q}{\mu_r m + q} \frac{e^{-hm}}{m}, \tag{4.38}$$

$$C_3 = \mu_2 \frac{\mu_0 I}{\pi} \frac{1}{\mu_r m + q} e^{-hm}. \tag{4.39}$$

Hence, the magnetic vector potential in the air and sheet region are given by

$$A_1(x,y) = \frac{\mu_0 I}{2\pi} \int_0^\infty \left(\frac{e^{my}}{m} + \frac{\mu_r m - q}{\mu_r m + q} \frac{e^{-my}}{m} \right) e^{-hm} \cos(mx)\, \mathrm{d}m, \tag{4.40}$$

$$A_2(x,y) = \frac{\mu_2 I}{\pi} \int_0^\infty \frac{e^{-hm} e^{qy}}{\mu_r m + q} \cos(mx)\, \mathrm{d}m. \tag{4.41}$$

The period-averaged Joule losses in the plate can be evaluated using the time-averaged Poynting vector

$$\boldsymbol{S} = \frac{1}{2} \boldsymbol{E} \times \boldsymbol{H}^*, \tag{4.42}$$

where $\boldsymbol{H}^*$ is the complex conjugate of the magnetic field intensity. To obtain the total complex power losses $P + \mathrm{j}Q$ in the plate, we need to integrate the projection of the Poynting vector in y-direction (pointing into the plate) over the surface

$$P + \mathrm{j}Q = \frac{1}{2} \int_{-\infty}^{\infty} (\boldsymbol{E} \times \boldsymbol{H}^*) \cdot \boldsymbol{e}_y \, \mathrm{d}x. \tag{4.43}$$

In the following, $\boldsymbol{e}_x$, $\boldsymbol{e}_y$ and $\boldsymbol{e}_z$ denote the unitary coordinate vectors. To transform (4.43) into an expression that can be easily evaluated with numerical tools, we express the Poynting vector in terms of the current density, which only has a component in z-direction

$$J = -\frac{\partial A_2}{\partial t} = -\mathrm{j}\omega\gamma A_2. \tag{4.44}$$

Using (4.44), the magnetic field intensity can be computed as

$$\boldsymbol{H} = \frac{1}{\mu} \nabla \times \boldsymbol{A}_2 = -\mathrm{j} \frac{1}{\omega\mu\gamma} \nabla \times \boldsymbol{J}. \tag{4.45}$$

Evaluating this for the vector components, the complex conjugate $\boldsymbol{H}^*$ of the magnetic field intensity is obtained as

$$\boldsymbol{H}^* = \mathrm{j}\frac{1}{\omega\mu\gamma}\left(\frac{\partial J^*}{\partial y}\boldsymbol{e}_x - \frac{\partial J^*}{\partial x}\boldsymbol{e}_y\right). \tag{4.46}$$

The electric field intensity is obtained from $\boldsymbol{J}$ by division through the conductivity γ

$$\boldsymbol{E} = \frac{J}{\gamma}\boldsymbol{e}_z. \tag{4.47}$$

Substituting (4.46) and (4.47) into (4.44) yields

$$P + \mathrm{j}Q = \frac{\mathrm{j}}{\gamma p^2}\int_0^\infty J\frac{\partial J^*}{\partial y}\,\mathrm{d}x. \tag{4.48}$$

Substituting the expression (4.44) in (4.48), an integral containing the product of two Fourier integrals is obtained that can be reduced to a single integral using Parseval's formula. The final expression for the complex losses is

$$P + \mathrm{j}Q = \mathrm{j}\frac{p^2 I^2}{2\pi\gamma}\int_0^\infty \frac{q^* e^{-2mh}}{(\mu_r m + q)(m u_r m + q^*)}\,\mathrm{d}x, \tag{4.49}$$

with q^* as the complex conjugate of q. The sheet resistance R_{sheet} can be directly computed from P, using $P = R_{\mathrm{sheet}} I^2$.

In order to check to what extent the derived analytical formula is useful in the context of induction heating of metal sheets, the analytical results are compared with numerical computations for the model shown in Fig. 4.5(b). As for all other considered induction heating setups in this thesis, a hollow, water-cooled inductor is used. Even though the sheet thickness is not infinite, it can be assumed that a metal plate whose thickness is greater than the skin depth at the given frequency will act essentially like a semi-infinite solid [49]. For the used material parameters ($\gamma = 9 \cdot 10^5 1/(\Omega\mathrm{m})$ and $\mu_r = 10$) the skin depth has the value δ =3.75mm at the minimum frequency of f =2kHz, so from a sheet thickness of $d = 4$mm on this assumption should be verified. First, the agreement between the analytically computed total losses P and the Joule losses in the sheet for different distances h were analyzed. Two different formulations for the current excitation are compared. For the A-formulation, the current density is constant over the inductor cross section, in analogy to the stranded coil approximation described in
Sec. 3.4. In the modified AV formulation, the skin effect in the inductor is taken into account. As shown in Fig. 4.6, there is a considerable difference between the analytical and numerical solution. An increasing distance leads to slight improvements, since the impact of the conductor geometry becomes less important if the conductor is further away from the plate. The difference between A and AV formulation is only noticeable for a coupling height of h = 10mm and frequencies above 50kHz. In that case, the currents will be strongly concentrated near the outer conductor surface, leading to slightly higher Joule losses in the sheet. From Fig. 4.7(a) it can be concluded that the previously stated assumption regarding the infinite sheet approximation is valid. In fact, from a sheet thickness of 5mm on, the curves for the numerically computed Joule losses are practically overlapping. The main reason for the important difference between analytical and numerical solution can be seen from Fig. 4.7(b): the limit for the validity of the analytical model resides in the finite spatial extension of the conductors. In other words, the current filament approximation can only be used for very small inductor widths and starts to converge towards the analytical results only for b_{ind} smaller than 1mm. Hence, 2D analytical solutions for the eddy currents induced in plates by current filaments are useful only to gain a qualitative overview on the problem. Also, one can see the large increase in complexity of the analytical solution even for the simplest possible two-dimensional case for sheet induction heating when the field distribution around the inductor is resolved.

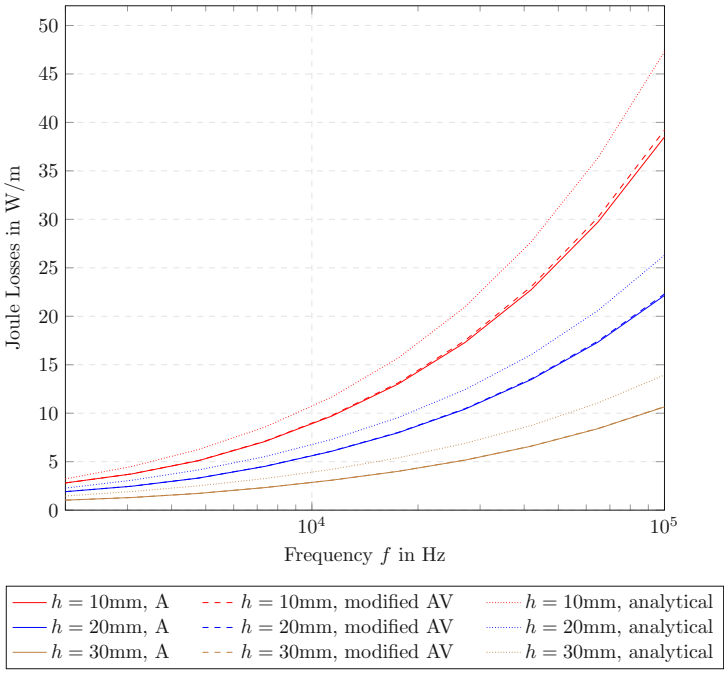

Figure 4.6: Influence of the distance between filament and plate for $b_{\text{ind}} = 5$mm and $d = 5$mm.

To sum things up, the difficulty to obtain a realistic value for the sheet resistance combined with the issues related to the analytical inductor resistance computations discussed in Sec. 4.1, stress the importance of numerical tools in the design of sheet heating applications.

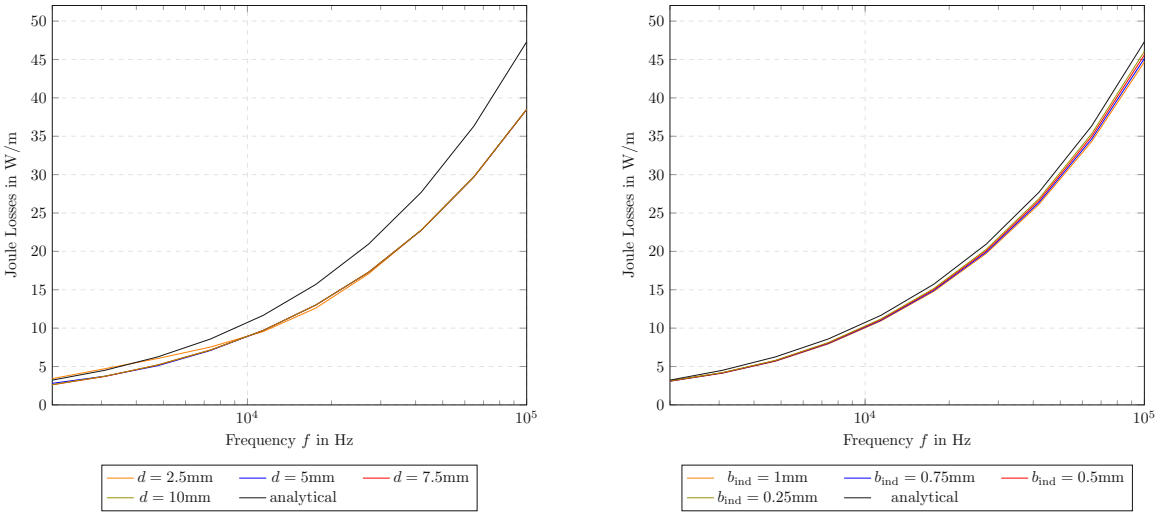

(a) Influence of the sheet thickness d for $b_{\text{ind}} = 5$mm.

(b) Influence of the conductor width b_{ind} for $d = 5$mm.

Figure 4.7: Models for a current filament over a plate.

Chapter 5

Efficiency Curves from Numerical Simulation

Now we want to obtain the actual efficiency curves for a LFH and a TFH setup. Two-dimensional (2D) and three-dimensional (3D) results are compared to see when the turning of the current at the sheet edge needs to be taken into account.

5.1 Computational Models

To start with, the assumptions used in the computational models will be discussed. Furthermore, the two and three-dimensional models will be validated through mesh convergence studies.

5.1.1 2D Models

The underlying assumptions for the two-dimensional model are that the sheet and the inductor have infinite length, such that the current is never turning in the sheet. In that case, the same setup of Fig. 5.1 can be used for both LFH and TFH. For the preparatory computations of this section, the coil is excited with a current of amplitude $\hat{I} = 60\text{A}$. The geometric dimensions and the material parameters used in the simulations are listed in Tab. 5.1 and Tab. 5.2 respectively.

Table 5.1: Geometry data for the LFH and TFH case according to Fig. 5.1, all dimensions in mm.

Setup	b_{ind}	h_{ind}	t_{ind}	l_{ind}	d	h_{coupling}
Longitudinal	15	25	1.5	150	2	10
Transverse	15	25	1.5	40	2	10

Table 5.2: Linear material parameters for the simulations.

Material	electric conductivity (in $(\Omega\text{m})^{-1}$)	permeability (in Vs/(Am))
steel	$9 \cdot 10^5$	$1.2566 \cdot 10^{-5}$
air	0	$1.2566 \cdot 10^{-6}$
copper	$5.67 \cdot 10^7$	$1.2566 \cdot 10^{-6}$

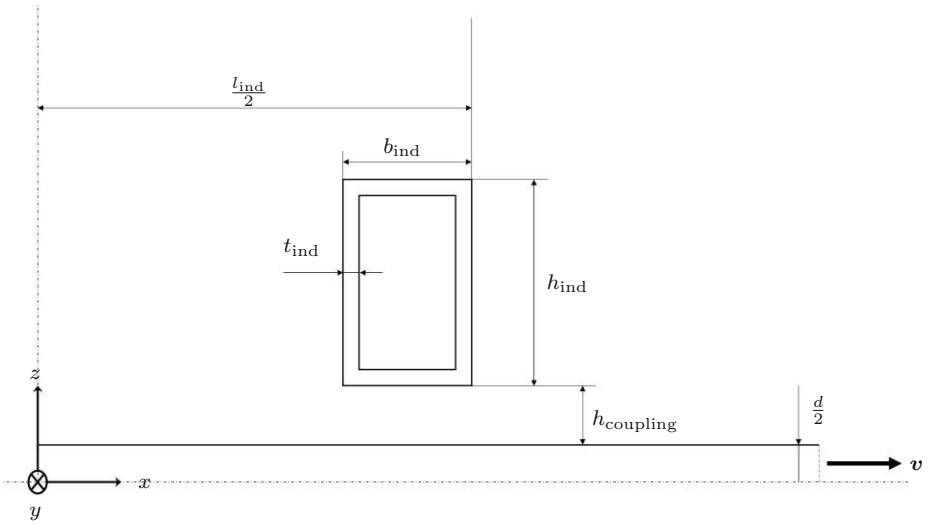

Figure 5.1: Setup with all relevant geometric dimensions.

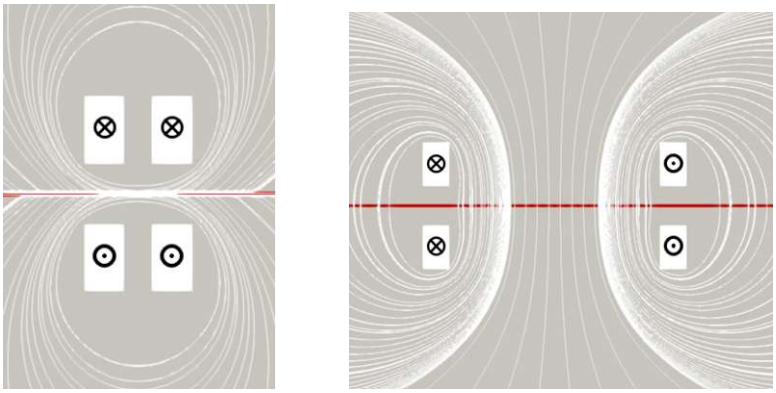

(a) Longitudinal Flux Heating.

(b) Transverse Flux Heating.

Figure 5.2: Comparison of magnetic field lines and current orientation for steel sheet heating setups.

The difference between the setups arises from the boundary conditions and the orientation of the current in the inductor. Modelling just a quarter of the setup is possible due to the 2 symmetry lines of the problem that can be seen from the magnetic field computations for the full model without any symmetry BCs in Fig. 5.2. Here the different flux situations are realized just by the orientation of the current: For the longitudinal case, one has to imagine a coil surrounding the sheet, while for the transverse case, there are inductors parallel to the sheet below and above the sheet.

When the magnetic field lines are tangential to the boundary, the boundary condition $\boldsymbol{B} \cdot \boldsymbol{n} = 0$ (for a normal vector $\boldsymbol{n}$) needs to be imposed. This corresponds to the x-y-plane for the longitudinal case and to the y-z-plane for the transverse case. For the other symmetry planes, the natural boundary condition $\boldsymbol{B} \cdot \boldsymbol{t} = 0$ (for a tangent vector $\boldsymbol{t}$) applies.

In the following, we will conduct some studies to find the optimal mesh settings for the 2D case. The structured mesh for the relevant regions is shown in Fig. 5.4(a). Since we are using edge elements with magnetic vector potential $\boldsymbol{A}$, the problem is pseudo-3D. Actually, $\boldsymbol{A}$ is normal to the 2D mesh plane, but it is constant in this direction, given that we consider a setup of infinite width. Thus, it is sufficient to just extrude the mesh with a single element in y-direction.

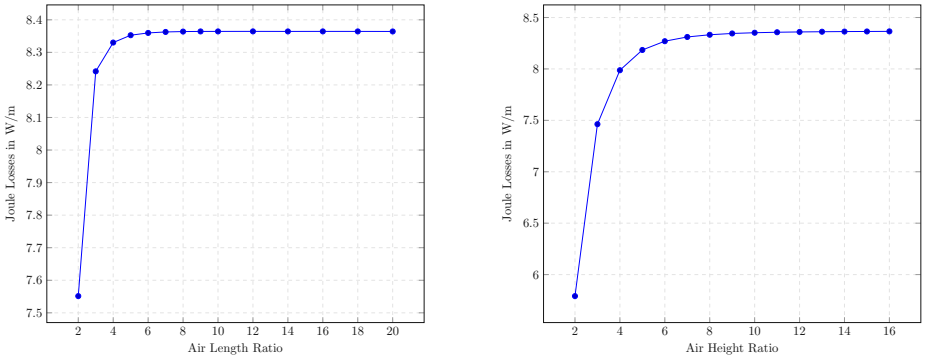

(a) Air length ratio $l_{\text{air}}/l_{\text{ref}}$. (b) Air height ratio $h_{\text{air}}/l_{\text{ref}}$.

Figure 5.3: Convergence study of the integrated Joule losses in the sheet for different air domain sizes, $l_{\text{ref}} = l_{\text{ind}}$ for the length ratio and $l_{\text{ref}} = d + 2h_{\text{coupling}} + 2h_{\text{ind}}$ for the height ratio.

Integrated Joule losses in the sheet are the evaluated quantity for the convergence study since they are one of the input values for the computation of the efficiency. They are evaluated at a single frequency, namely a value close to the optimal efficient frequency that will be determined in the next section. For the LFH case, the evaluation frequency is 50kHz, for the TFH setup 5kHz. Note that it is sufficient to conduct one study for both setups, as due to the symmetry considerations discussed in the previous point the mesh structure is exactly the same for the longitudinal and the transverse case. In a first step, we need to determine the minimal size of the air domain to get reliable results. The dimensions of the air domain are shown in Fig. 5.5(a). For the 2D case, the actual air width is not important, given that we only have a pseudo-3D problem. A sheet width of 1m is chosen such that we immediately get the results in W/m. Two separate convergence studies were conducted for the size of the air domain with respect to the inductor dimensions. The results are shown in Fig. 5.3. For the air length ratio in Fig. 5.3(a), the inductor length $l_{\text{ref}} = l_{\text{ind}}$ is chosen for reference. A length ratio of 6 is sufficient to achieve a converged result. The reference for the air height ratio as shown in Fig. 5.3(b) is the total height of the setup, given by $l_{\text{ref}} = d + 2h_{\text{coupling}} + 2h_{\text{ind}}$. A height ratio of 8 is chosen in the following.

For the mesh refinement study in Fig. 5.4(b), the characteristic length is the circumferential element size of the inductor cross section. All other grid sizes are chosen proportional to this reference length. Note that a bias is applied in the sheet and in the inductor, where we need to resolve the skin depth, because otherwise an acceptable convergence rate cannot be realized.

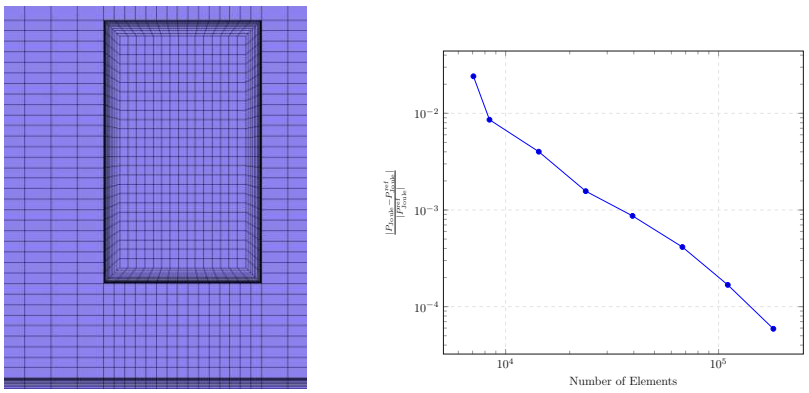

(a) Structured mesh of inductor and sheet. (b) h-refinement using lowest order elements.

Figure 5.4: Mesh refinement study for the 2D setup.

5.1.2 3D Models

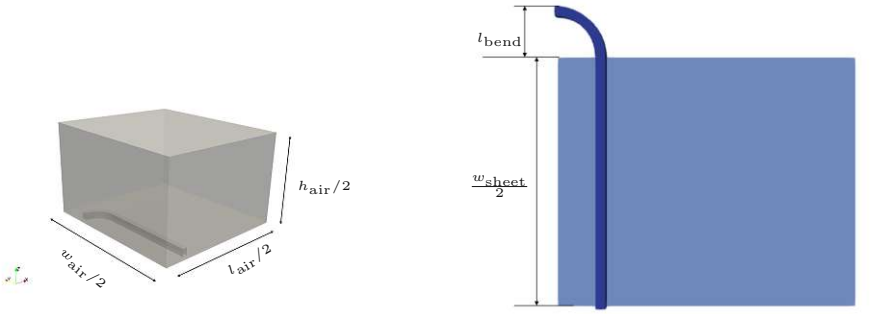

(a) Air domain dimensions.

(b) Definition of 3D geometry parameters.

Figure 5.5: Definition of geometry parameters for the 3D setup.

For the 3D models, the geometry of the inductor in y-direction is taken into account, so different models are required for the longitudinal and transverse setup, even though the same symmetries and boundary conditions are applied. In 3D, another symmetry can be applied for the magnetic problem as well as for the heat problem, namely the symmetry with respect to the y-z-plane, as shown in Fig. 5.5. Pyramid elements are not implemented in openCFS, such that transitions between hexahedral (hex) and tetrahedral (tet) elements are not possible in a conforming way. The regions where the skin depth must be resolved should be meshed with hexahedral elements. Close to the surface there will be elements with a very high aspect ratio for the mesh size in depth direction (y-direction) compared to the mesh size in the cross-sectional direction (in the x-z plane). For transformations from the reference elements to the physical space for the curl operator, a division by the element Jacobian is necessary. Tetrahedral elements have a much smaller Jacobian compared to hexahedral ones, so for unfavourable aspect ratios they are more liable to cause numerical difficulties. Moreover, regarding non-conforming interfaces, the most accurate results are obtained for hex-hex combinations. Hence, an all hexahedral mesh was created. For LFH, the turn of the inductor is always located outside of the sheet, so a fully conforming hex mesh is possible, as shown in Fig. 5.6(a). For TFH, a fully conforming mesh is only possible when the turn is located outside of the sheet, but since in general this is not realized, a non-conforming mesh is necessary. However, one must take care not to put the non-conforming interface at a point with a permeability jump, since this might cause inaccurate results. Thus, a good solution is to locate the non-conforming interface in the middle of the air-gap between inductor and sheet. The top part with the inductor and the bottom part with the sheet can be meshed separately in a fully structured way. A top view of the upper part of the mesh with the inductor can be seen in Fig. 5.6(b).

In the 3D case, the optimal air width as defined in Fig. 5.5(a) also needs to be determined. The same procedure as for the 2D case is adopted, fixing the air width and height to the optimal values chosen according to Fig. 5.3 and varying the air domain width. The reference value for the computation of the air width ratio is the total inductor length, given by $w_{\mathrm{sheet}} + 2l_{\mathrm{bend}}$, as defined in Fig. 5.5(b). Comparing the maximum changes in the values of the integrated Joule losses of the studies for the 2D air dimensions in Fig. 5.5(a) with the ones for the air width according to Fig. 5.7, the changes are less important and the additional gain in precision is small compared to the increase in computational resources. In the end, an air width ratio of 1.5 is chosen because from that value on the curve is flattening out.

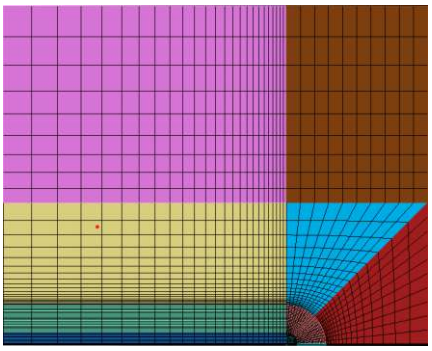

(a) Lateral view of the mesh for the longitudinal setup.

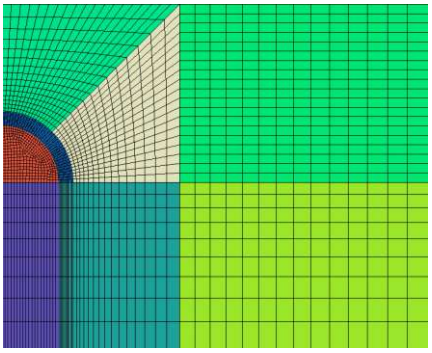

(b) Top view of the mesh for the transverse setup.

Figure 5.6: Structured hex meshes for the 3D simulations.

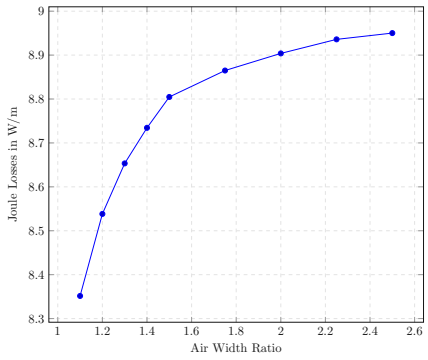

Figure 5.7: Convergence study of the integrated Joule losses in the sheet for different air width ratios $w_{\text{air}}/l_{\text{ref}}$, with $l_{\text{ref}} = w_{\text{sheet}} + 2l_{\text{bend}}$.

For the 3D mesh refinement we proceed in an analogous way as for the 2D case, but this time also a refinement in depth direction is required. Especially the turns and the sheet edges have to be meshed with a sufficient number of elements since the change in the direction of the currents needs to be resolved. For a good convergence rate, it is favourable to apply a bias in the sheet width direction, such that we have smaller elements close to the edge and larger elements towards the middle of the sheet, where no significant gradients in y-direction occur. The results are shown in Fig. 5.8.

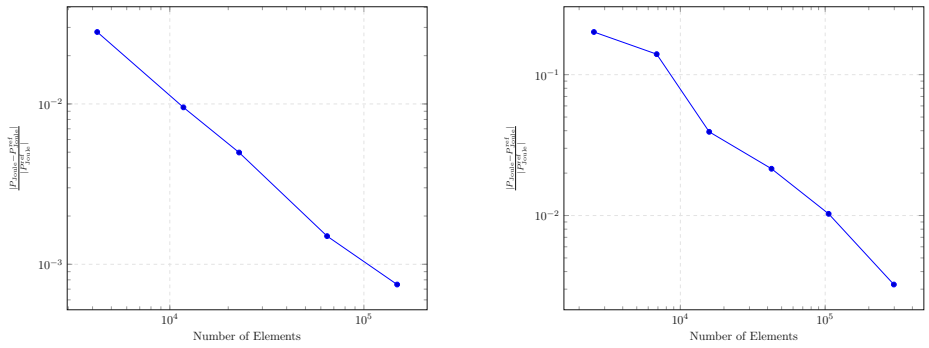

(a) h-refinement study LFH.

(b) h-refinement study TFH.

Figure 5.8: Mesh-refinement study for 3D models, using lowest order elements.

One of the most important questions regarding modelling is the validity range of the reduction of the full 3D setup to the computationally cheaper 2D case. While this question will be analyzed through direct comparison of efficiency curves and field values in the next section, an interesting point is the influence of the sheet width on the electromagnetic results, namely from what sheet width on the assumption of an infinite sheet is justified. The evaluated criterion is the convergence of the integrated Joule losses, as well as the x component of the magnetic flux density B_x, at the surface of the sheet, close to its centre, where the disturbances from the edge have disappeared and the 2D assumption should be valid. In literature, the region where the influence of edge effects on the electromagnetic field values is negligible is referred to as the regular zone. For TFH it is fully developed from ratios of $w_{\text{sheet}}/l_{\text{ind}} > 2$ [47]. Given that $l_{\text{ind}} = 0.15\text{m}$ for the TFH setup, this agrees reasonably well with the results of the magnetic flux density at the sheet surface, shown in Fig. 5.10(b), where from $w_{\text{sheet}} = 0.5\text{m}$ on, the value of B_x is close to the 2D one, while for $w_{\text{sheet}} = 0.25\text{m}$, there is still a significant difference. A similar convergence behaviour is obtained for the magnetic flux density in the LFH setup, shown in Fig. 5.9(b). For the integrated Joule losses plotted in Fig. 5.9(a) and Fig. 5.10(a), convergence is much slower and the actual 2D values are not reached within a reasonable value range of the sheet width. On the one hand, this is caused by the increased Joule losses close to the edges, on the other hand, the active power input to the system is also higher for the 3D case due to the presence of the turn.

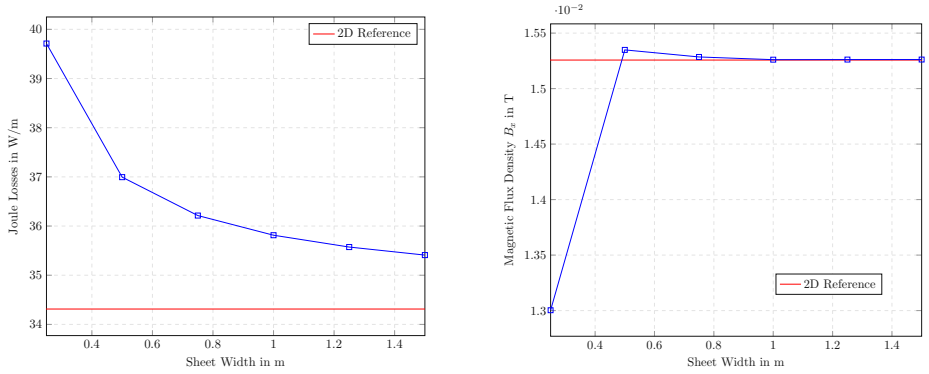

(a) Integrated Joule losses. (b) Magnetic flux density.

Figure 5.9: Influence of the sheet width for LFH with comparison to the values from 2D computations.

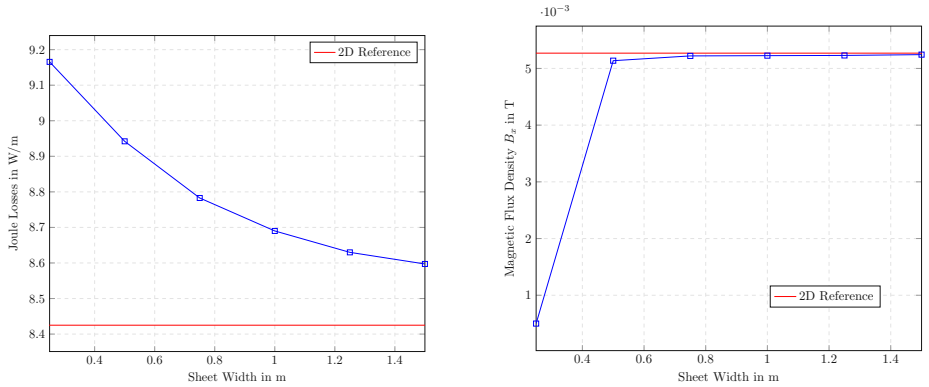

(a) Integrated Joule losses. (b) Magnetic flux density.

Figure 5.10: Influence of the sheet width for TFH with comparison to the values from 2D computations.

5.2 Results

In the following, the electromagnetic field quantities will be computed over a wider frequency range, such that curves for the electrical efficiency and the power factor over the excitation frequency can be obtained. Furthermore, the field values in the sheet will be analyzed at different frequencies, to evaluate the impact of the skin effect and understand its influence on the efficiency measures. 2D and 3D results will be directly compared. In industrial induction heating applications, input powers ranging from 1kW to 10MW and frequencies in the range from 50Hz to 1MHz can be found [1]. To obtain more realistic power values, the excitation current is increased to $\hat{I} = 2.5\text{kA}$.

5.2.1 Longitudinal Flux Heating

The curves for the electrical efficiency measures are given in Fig. 5.11. To compute the efficiency curves, 100 frequency points with logarithmic distribution were computed. Based on that, an interval for the optimal frequency could be derived. Within this interval, the values given in Tab. 5.3 were determined, with a frequency resolution of 50Hz. For the electrical efficiency η, there is no clear maximum because after reaching a certain maximal value it is practically constant. The power factor has a distinct maximum and consequently is the best indicator for the optimal frequency in this case. As indicated in Sec. 2.5, the value of the maximum power factor is small for LFH setups.

Table 5.3: Optimal efficiency values for LFH setup.

Setup	f in kHz	η in %	$\cos(\varphi)$
2D	50.1	93.1	0.154
3D	49.9	92.9	0.160

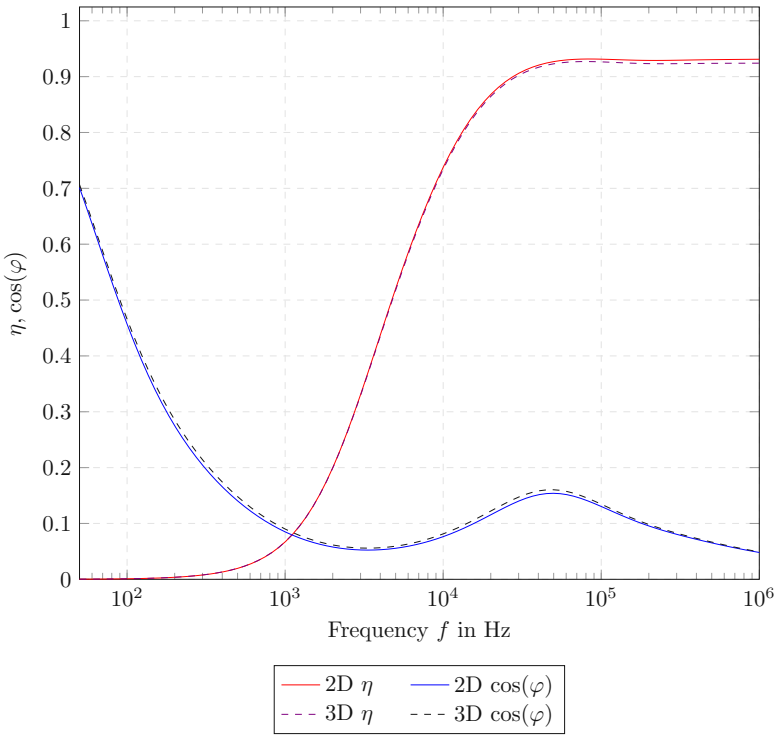

Figure 5.11: Electrical efficiency η and power factor $\cos(\varphi)$ over the excitation frequency for LFH.

The flattening out of the efficiency curve can be directly obtained from the analytical formula for the Joule losses in the sheet for inverse currents (4.25): the frequency dependency is $\sqrt{f}\lambda_{\mathrm{LFH}}$. The proportionality from the square root of the frequency f comes from the inverse dependency on the skin depth δ. As discussed in Sec. 4.1, the inductor resistance has a similar dependency. Consequently, once λ_{LFH} approaches a fixed value, there will be no further increase in efficiency. In fact, there is even a slight efficiency decrease for higher frequencies because some secondary influences on the inductor resistance lead to higher losses in the coil [1]. In the 3D case, this effect is more pronounced, because the turn located outside of the sheet contributes to the coil losses without further increasing the Joule losses in the sheet.

The curves for the 2D and 3D case are practically overlapping over the whole frequency range and also the difference between the optimal frequencies and maximum efficiency values are negligible, which is plausible since no important 3D effects are expected in the LFH case. As predicted by Fig. 2.3(a), the sheet currents are circulating in the x-z-plane. The turning of the currents near the sheet edge is illustrated in Fig. 5.12. It can be seen that a deviation from the 2D current profile, which can only have a y-component, is occurring only in a section near the sheet edge of 1/20 of the sheet width.

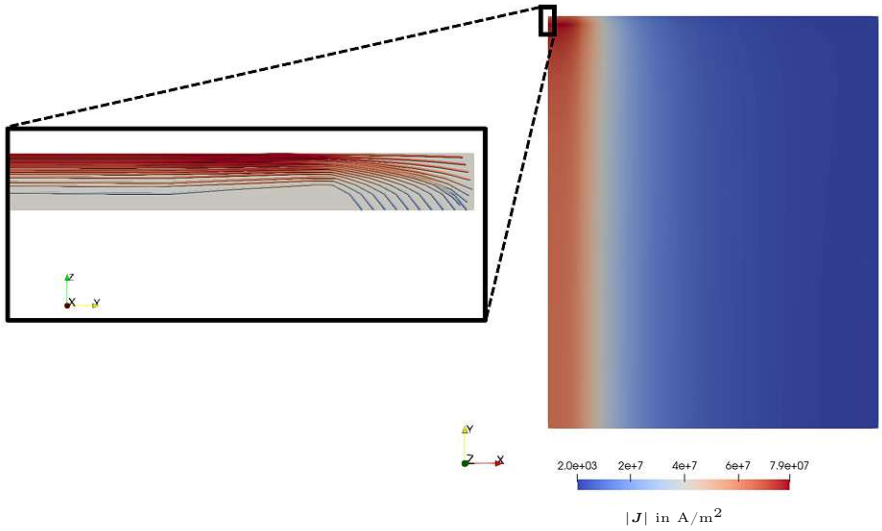

Figure 5.12: Sheet current density distribution for LFH at $f = 50$kHz, detailed view of the current path at the sheet edge.

In Fig. 5.13, the electromagnetic field quantities are evaluated over the sheet thickness for different frequencies. As shown analytically in Fig. 4.3(a), the eddy current density in the middle of the sheet is vanishing, with the maximum value at the sheet surface. For $f = 5$kHz, the skin depth is $\delta = 2.37$mm and the ratio d/δ is smaller than 1, so the magnetic flux density is practically constant over the sheet thickness. For higher frequencies, the distribution of the magnetic flux density will become increasingly uneven due to the skin effect. For frequencies one order of magnitude higher than the optimal frequency, there is even a negative magnetic flux density and a negative eddy current density towards the plate centre. No significant differences between the 2D and 3D computations can be detected.

The distribution of the field values over the length of the sheet is shown in Fig. 5.14. In the area between the inductor wires, the current density is constant for the optimal frequency, as visualized in Fig. 5.14(b).

Consequently, the induced power density is homogeneously distributed over the coil length without any significant peaks, which is favourable as there is a limit for the maximum power density that can be securely transferred to the sheet. Exceeding that limit, the resulting electromagnetic forces can lead to significant mechanical effects, such as vibrations or noise emission [47]. The qualitative behaviour of the x-component of the magnetic flux density is the same as for the current density J_y.

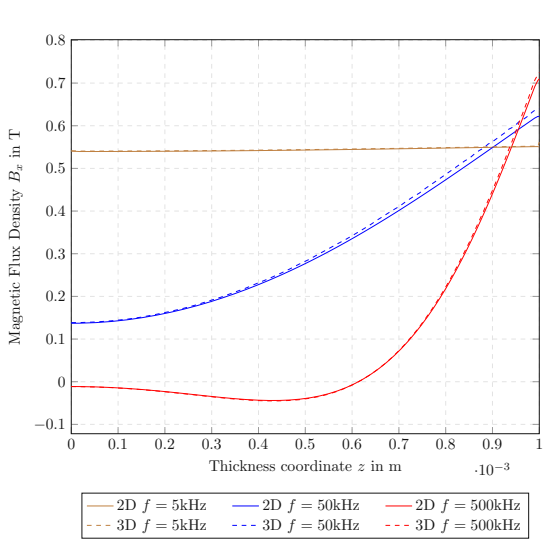

(a) x-component of the magnetic flux density B_x.

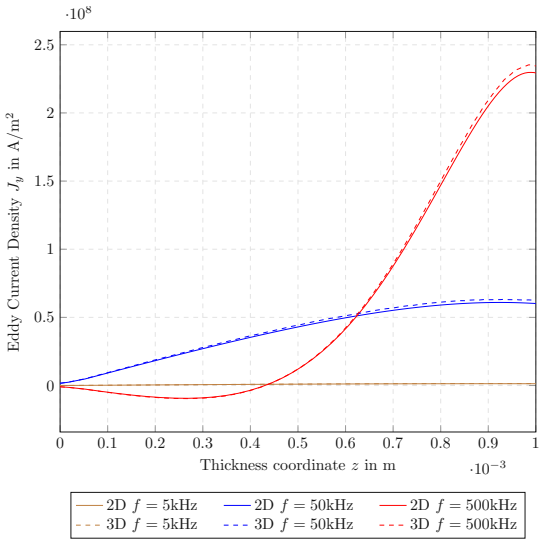

(b) y-component of the eddy current density J_y.

Figure 5.13: Comparison of field results from 2D and 3D computations over sheet thickness for LFH, for different frequencies. The field quantities are evaluated right below the inductor centre, close to the middle of the sheet. The sheet surface is at $z = 1$mm.

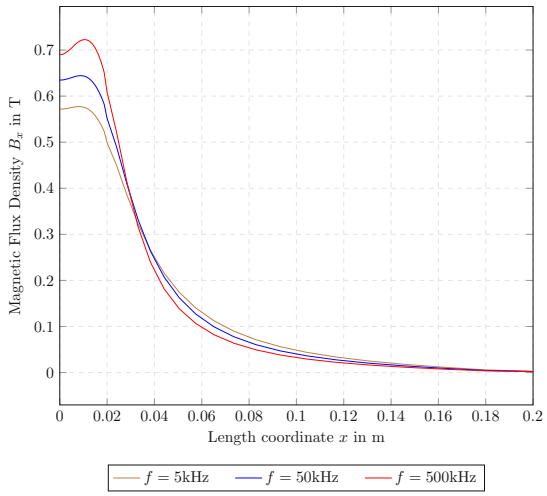

(a) x-component of the magnetic flux density B_x.

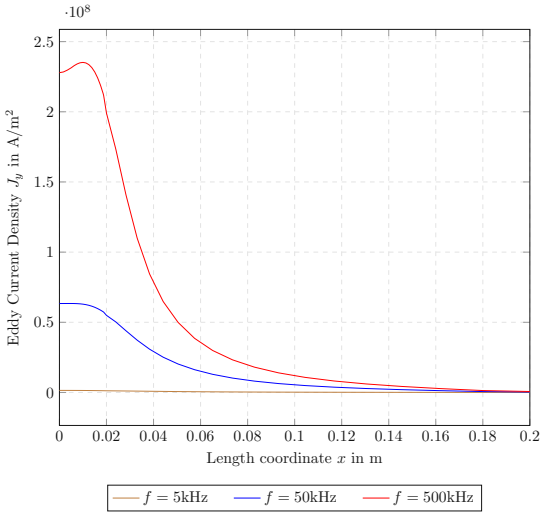

(b) y-component of the eddy current density J_y.

Figure 5.14: Field results from 2D computations over sheet length for LFH, for different frequencies. The field quantities are evaluated at the sheet surface at $z = 1$mm. The symmetry plane is at $x = 0$mm.

5.2.2 Transverse Flux Heating

For TFH setups, there is a clear maximum of the electrical efficiency besides the maximum of the power factor, as can be seen from Fig. 5.15. According to Tab. 5.4, the maximum power factor and maximum efficiency are not occurring at the same frequency, even though the deviations for the optimal values are negligibly small. Compared to the efficiency curves for the longitudinal case in Fig. 5.11, the differences between the 2D and 3D computations are much more important. This is expected, since the turning of the current at the sheet edge below the inductor turn introduces 3D effects over a large part of the sheet width, which cannot be modelled by the infinite sheet width assumption of the 2D setup.

Table 5.4: Optimal efficiency values for TFH setup.

Setup	Maximum η			Maximum $\cos(\varphi)$		
	f in kHz	η in %	$\cos(\varphi)$	f in kHz	η in %	$\cos(\varphi)$
2D	5.1	93.8	0.394	3.85	93.6	0.399
3D	5.3	93.2	0.365	4.65	93.1	0.369

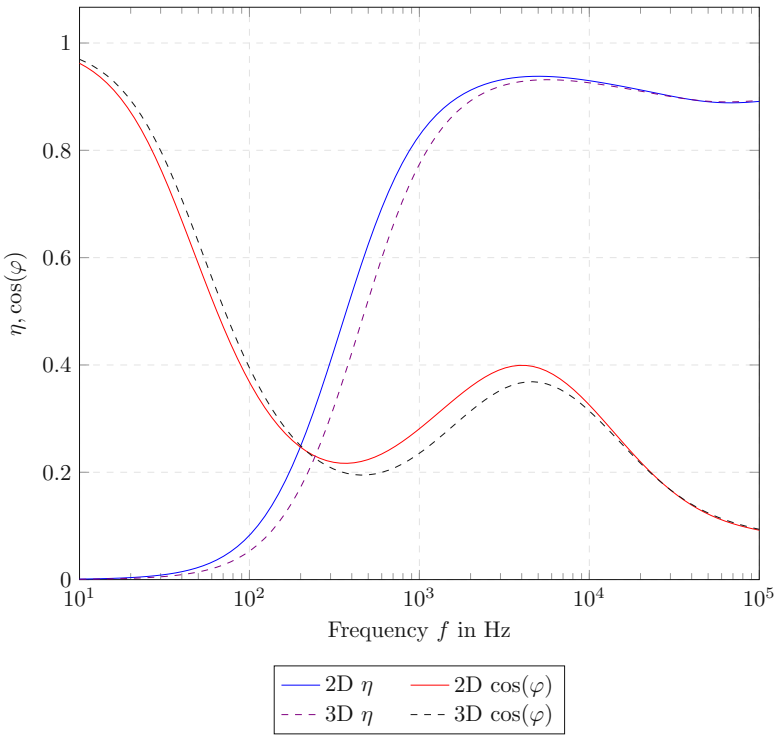

Figure 5.15: Electrical efficiency η and power factor $\cos(\varphi)$ over the excitation frequency for TFH.

The currents in the sheet are the inverse image of the currents in the inductor, which is also illustrated in Fig. 5.16. They follow the shape of the turn and they are mainly concentrated below the inductor. Regarding the distribution of the field quantities over the sheet thickness Fig. 5.17, the x-component of the magnetic flux density is vanishing in the centre of the plate, as predicted analytically by applying symmetry considerations to the case of currents of same direction on both sides of the sheet in (4.13). For ratios of d/δ smaller than 1, the eddy current density is constant over the sheet thickness as could also be shown based on analytical results in Fig. 4.3(b).

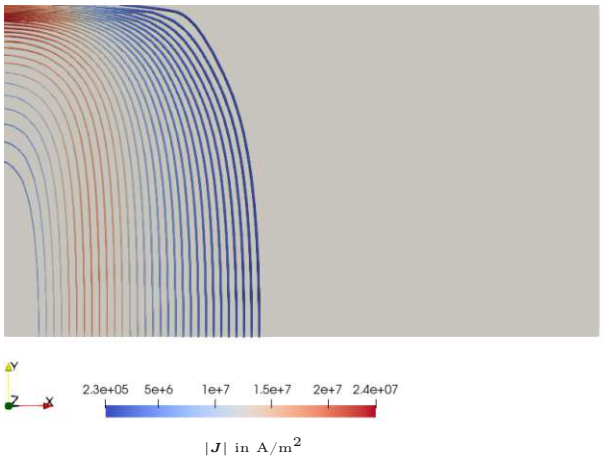

Figure 5.16: Current path in the sheet for TFH at $f = 5\text{kHz}$, view in z-direction.

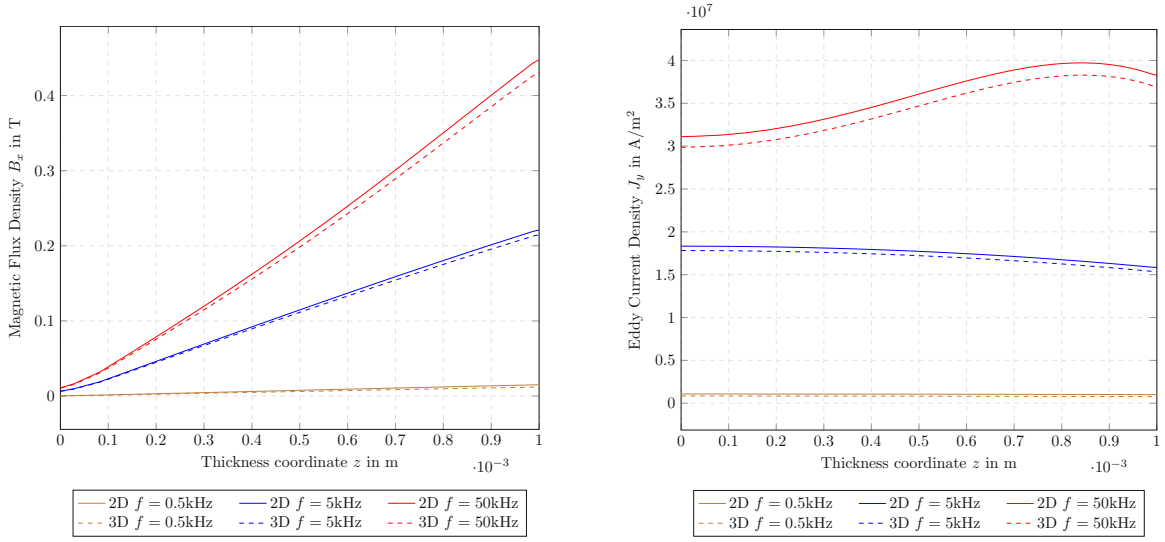

(a) x-component of the magnetic flux density B_x.

(b) y-component of the eddy current density J_y.

Figure 5.17: Comparison of field results from 2D and 3D computations over sheet thickness for TFH, for different frequencies. The field quantities are evaluated right below the inductor centre, close to the middle of the sheet. The sheet surface is at $z = 1\text{mm}$.

The reason for the different curvature of the eddy current density plots between Fig. 5.17(b) and Fig. 4.3(b) can be derived when considering the distribution of the magnetic flux density components over the sheet length Fig. 5.18: the analytical model from Sec. 4.2 considers only components of the magnetic field in x-direction. However, at ratios d/δ smaller than 1, there is an important magnetic flux normal to the plate surface, the so-called "transverse flux". For higher frequencies, the induced currents in the sheet cause an opposite magnetic field in the z-direction, such that the useful transverse magnetic flux between the inductors becomes practically zero, as it is the case for $f = 50\text{kHz}$ in Fig. 5.18(b). At that point, the situation of the field values in the plate becomes similar to that of the longitudinal case, with a reorientation of the magnetic flux density parallel to the sheet surface, as the sheet becomes less and less transparent to the magnetic field due to the skin effect. Similarly, the distribution of the eddy currents inside the sheet is more uneven, with a maximum close to the sheet surface.

For the eddy current distribution over the sheet length Fig. 5.19(a), one notices a strong concentration of the currents below the inductor. In the centre between the inductors the current density component J_y has to completely vanish, given that the currents in the two inductor branches must be opposed. In fact, for a qualitative description of the situation, the total current distribution in the sheet is commonly reduced to a constant current density circulating in the sheet in a cross-section of dimensions sheet thickness times inductor width [47]. This agrees well with the simulation results. Fig. 5.19(b) illustrates the notion of regular zone introduced previously: for a third of the plate width, the current density has only a y-component. In that region, the field values over the sheet length and thickness can be described by the 2D model, an assumption that is confirmed by the good accordance between 2D and 3D results in Fig. 5.17.

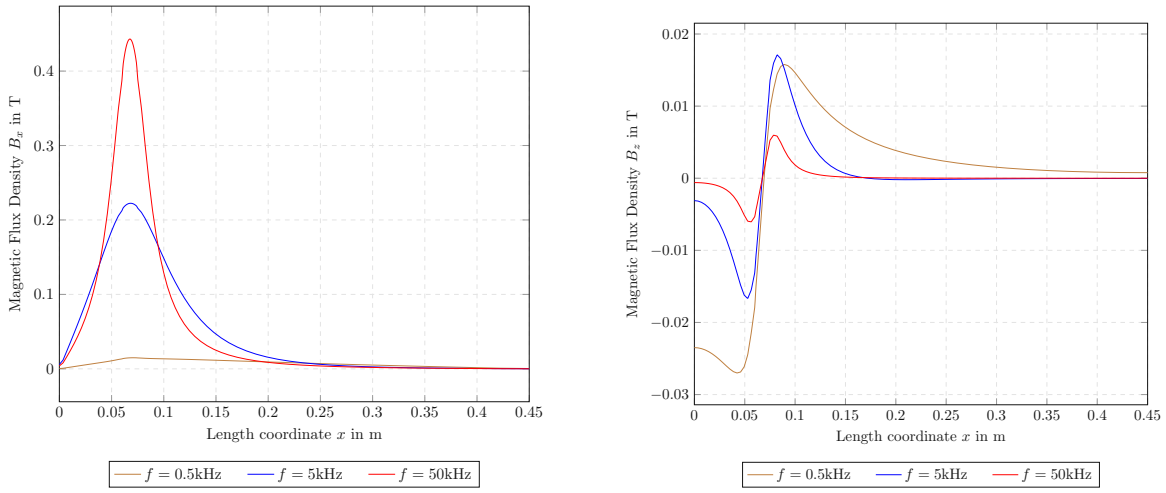

(a) x-component of the magnetic flux density B_x.

(b) z-component of the magnetic flux density B_z.

Figure 5.18: Magnetic Flux density from 2D computations over sheet length for TFH, for different frequencies. The field quantities are evaluated at the sheet surface at $z = 1$mm. The symmetry plane is at $x = 0$mm.

Closer towards the sheet edges, the currents are turning, resulting in currents in x-direction of maximum values as large as one half of the J_y currents. This reorientation of the sheet currents close to the sheet edge leads to an important current density concentration as visualized in Fig. 5.16, resulting in the potentially problematic edge overheating effects. One important design parameter in that regard is the position of the bend centre relative to the sheet edge. The optimal frequency and maximum attained efficiency for different bend positions l_{bend} (as defined in Fig. 5.5) are studied in Fig. 5.20. For a better interpretation of the results, it should be noted that the turn radius is equal to $l_{\text{ind}}/2 = 75$mm, so that for $l_{\text{bend}} > 75$mm, the turn is located completely outside the sheet. Concerning the optimal frequency, no clear trend could be found, as the values are distributed more or less randomly in the range between 5.2KHz and 5.6KHz. The maximal electrical efficiency is reached for $l_{\text{bend}} = 0$mm, with a strong decrease the more the turn is located outside of the sheet. In that case, a large portion of the inductor is not located in the sheet plane and consequently does not contribute to the Joule losses, while it is still causing an increasing electrical resistance.

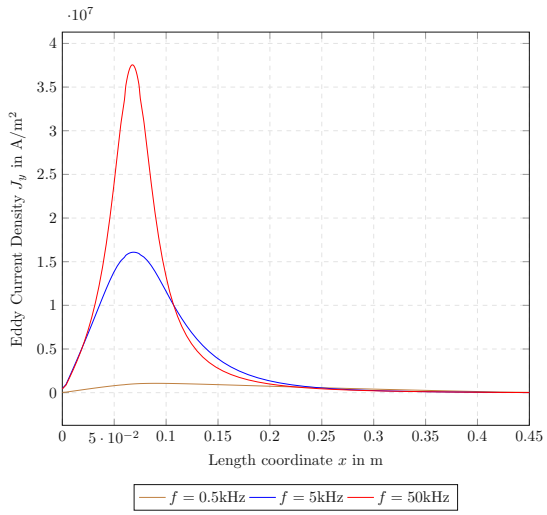

(a) y-component of the eddy current density J_y over sheet length.

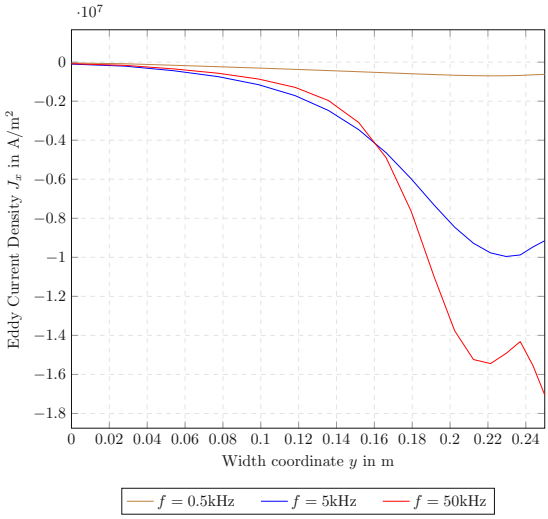

(b) x-component of the eddy current density J_x over sheet width.

Figure 5.19: Current density over sheet length (2D computations) and sheet width (3D computations) for TFH. The symmetry plane is at $x = 0$mm and $y = 0$mm respectively.

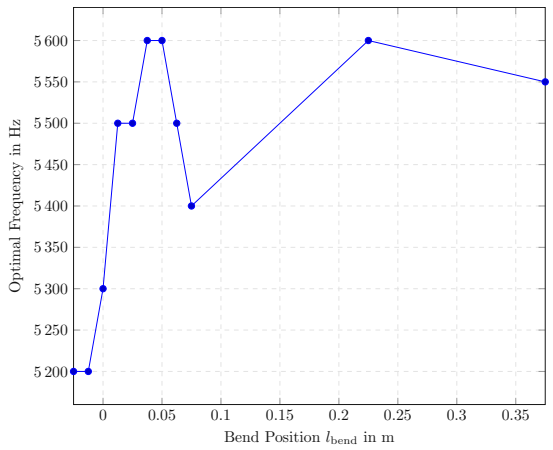

(a) Optimal frequency for different bend positions l_{bend}.

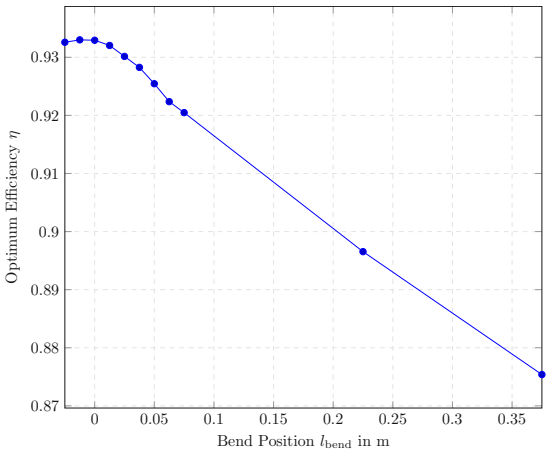

(b) Optimal efficiency for different bend positions l_{bend}.

Figure 5.20: Influence of the bend position l_{bend} on the electrical efficiency.

For a complete investigation of edge effects in TFH, a heat simulation must be conducted. Now, the sheet velocity must be taken into account due to the advection term of the heat PDE. A sheet velocity in x-direction of $v_x = 0.1$m/s is chosen, the other simulation parameters are summarized in Tab. 5.5.

Table 5.5: Parameters for the thermal simulation in the sheet.

density (in kg/m^3)	heat conduction (in W/(mK))	heat capacity (in J/(kgK))	heat transfer coefficient (in W/(m^{2}K))	inlet temperature (in °C)	bulk temperature (in °C)
7860	510	15	15	20	20

The inlet temperature is fixed, while at the outlet and at all symmetry planes, zero heat flux is set. For the contact surfaces with the air region, convective heat transport with a constant heat transfer coefficient is assumed. The advection term breaks the symmetry with respect to the y-z-plane, so that the temperature field has to be computed on the half model instead of the quarter one. The results for the temperature field Fig. 5.21 show a clear temperature maximum close to the sheet edge. To analyze the effect of the bend position on edge overheating, the temperature distributions along the sheet width were compared in Fig. 5.22 for different bend positions. If the edge of the turn is located inside the sheet, the lowest edge overheating is observed and the the maximum temperature is found at a certain distance from the sheet edge. Moving the bend outside of the sheet, the maximum temperature increases up to a bend position of one half of the bend radius, while for larger values of l_{bend}, the maximum is decreasing again. Hence, the strongest concentration of eddy currents at the sheet edge is not appearing when the bend is placed completely inside the sheet plane, but when half of the turn is located outside of the sheet. As already mentioned, the currents inside the sheet are the mirror of the inductor currents. However, when the turn is located outside of the sheet, the sheet currents will still be forced to turn at the sheet edge.

Now, the turning will start closer to the sheet edge and the corresponding eddy current density will be higher. This can deduced from Fig. 5.22(a): for $l_{\text{bend}} = 0\text{mm}$, the temperature increase starts already at a width coordinate $y = 0.18\text{m}$, whereas for $l_{\text{bend}} = 37.5\text{mm}$, there is a steeper temperature rise only from $y = 0.22\text{m}$ on. The decrease of the maximum temperature for bend positions further away from the sheet is caused by the drop in electrical efficiency. In this context it should be noted that a reasonable edge overheating is sometimes desired, since the sheet edges are cooling faster than the rest; an effect that could not be taken into account by our assumption of a uniform inlet temperature. Still, for our case the best compromise for a high electrical efficiency and a homogeneous temperature distribution were obtained for a bend position of $l_{\text{bend}} = 0\text{mm}$, where the bend is lying completely in the sheet plane. This configuration will also be used for the parameter studies in the next chapter.

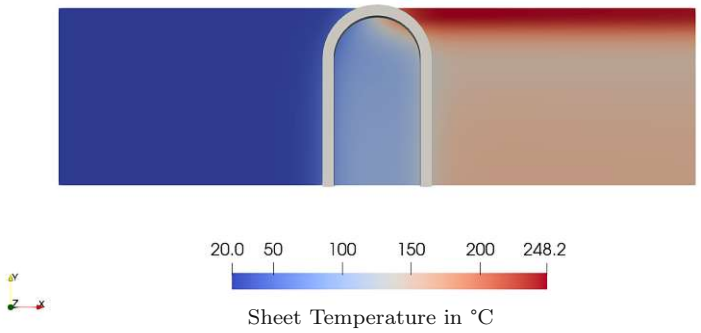

Figure 5.21: Temperature distribution at the sheet surface for TFH.

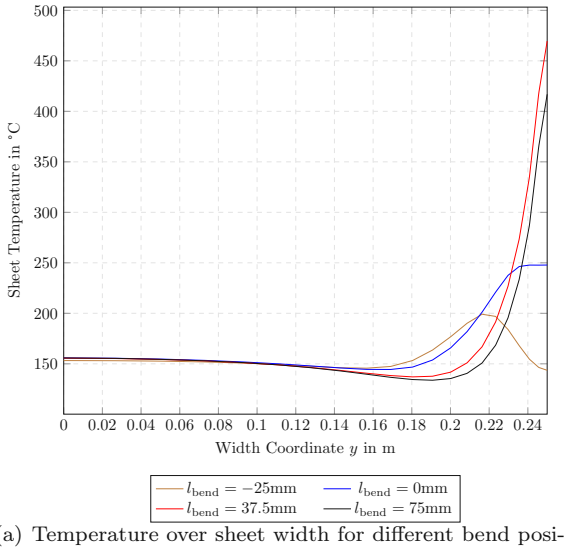

(a) Temperature over sheet width for different bend positions.

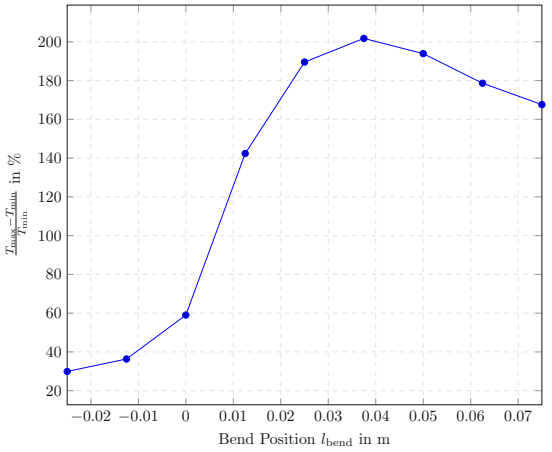

(b) Maximum relative temperature difference for different bend positions.

Figure 5.22: Influence of the bend position l_{bend} on the temperature distribution at the sheet surface.

Chapter 6

Influence of Geometry and Material on Efficiency

In this chapter, the dependencies of the optimal frequency and maximum efficiency will be studied for geometric design parameters and sheet data, namely the sheet thickness and its material parameters. For LFH, only 2D computations were performed, since the results found previously do not indicate any important 3D effects in that case, so that the optimal frequency prediction is assumed to be valid also for the full 3D setup. For TFH, though, the effects in the edge region have a noticeable impact on the efficiency curves, so the 2D results were compared with 3D computations. In the 2D case, the optimization algorithm of golden section search [50] was used to find the optimal frequency with an accuracy of 0.1%. For the 3D results, if used, a reduced frequency interval was introduced, typically ranging from the 2D optimal frequency to a frequency value 30% higher than the optimal frequency with a frequency resolution of 50Hz. In the conducted studies the frequencies in the 3D case were always higher than their 2D equivalents; if the optimum was found at an interval boundary, the study domain was extended.

6.1 Longitudinal Flux Heating

Considering the results from Sec. 4.2, in particular Fig. 4.2, the optimal efficiency is reached approximately for a ratio d/δ=2.7, from which an approximate of the optimal efficiency can be derived as

$$f_{\text{opt}} \approx \frac{7.29}{\pi d^2 \mu \gamma}. \tag{6.1}$$

This formula is used only to check if the qualitative dependencies are the same for the numerical results, an accurate prediction over the whole parameter range cannot be expected from such a simplified approach. As discussed in Sec. 2.5, the d/δ values used in industrial sheet heating applications vary over a wider range. For the heating of a cylindrical body inside a coil, the following estimate of the maximum efficiency can be obtained from (4.1) [1]

$$\eta_{\text{opt}} \approx \frac{1}{1+\alpha\sqrt{\frac{\gamma}{\gamma_{\text{i}}\mu}}}, \tag{6.2}$$

where α is the coupling ratio defined as ratio between the internal diameter of the inductor and the external diameter of the heated cylinder and γ_{i} is the conductivity of the inductor. Even though the definition of α cannot be directly transferred to the case of sheets, experimental data in [1] proves that the qualitative behaviour is the same for slabs. The default settings in the following parameter studies are those from Tab. 5.1 for the geometry and Tab. 5.2 for the material data.

For the influence of the sheet thickness Fig. 6.1, the optimal frequency varies with $\frac{1}{d^2}$. The maximum efficiency is constant which corresponds to the results found in [51]. The small fluctuations are due to the fact that for LFH the maximum power factor has to be used for determining the optimal efficiency because the efficiency curve does not have a distinct maximum. In some cases, the maximum power factor is reached for slightly lower frequencies than the plateau for the maximal efficiency, causing some oscillations in the maximum efficiency results. The increase of the power factor for larger sheet thicknesses can be explained by the frequency dependency of the reactances in the system. Higher sheet thicknesses lead to lower optimal frequencies, smaller reactive power and imply a higher power factor.

With an increasing coupling height, the optimal frequency diminishes, while the maximum efficiency and power factor are also decreasing, as shown in Fig. 6.2. In the case of a coil surrounding the sheet, the influence of the coupling height on the magnetic field strength should be very small. The efficiency decrease is rather related to the higher stray losses in the larger air gap and to higher return path losses. Generally, the coupling height is chosen as small as possible, but there are always constraints to assure the safe transport of the sheets through the inductor and to avoid collisions. The chosen security margin depends on the sheet velocity, temperature increase, thermal expansion coefficient and also on the general process layout, e.g., the distance to other processing steps [15].

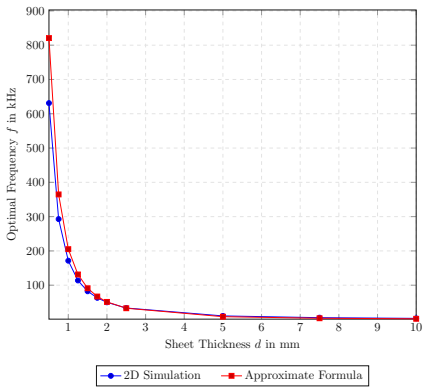

(a) Optimal frequency.

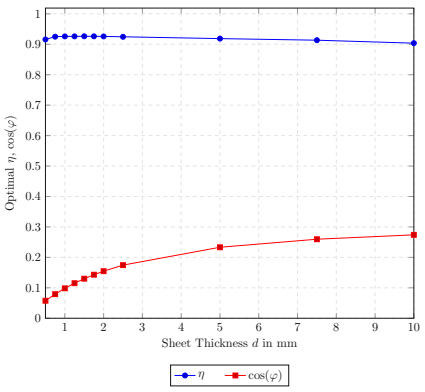

(b) Efficiency and power factor at optimal frequency.

Figure 6.1: Influence of sheet thickness d on efficiency for LFH.

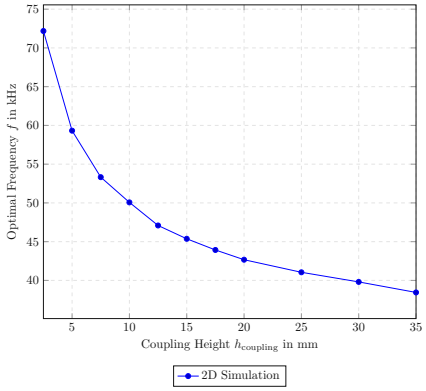

(a) Optimal frequency.

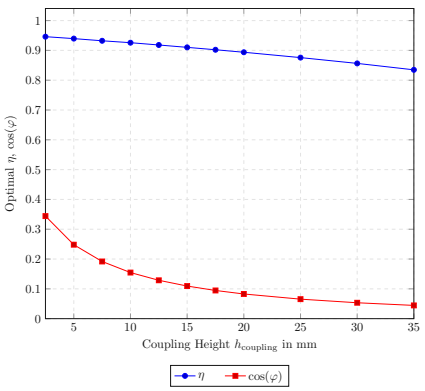

(b) Efficiency and power factor at optimal frequency.

Figure 6.2: Influence of coupling height h_{coupling} on efficiency for LFH.

Regarding the dependency on the sheet conductivity and permeability in Fig. 6.3 and Fig. 6.4, we have an inverse dependency of the optimal frequency on the respective material parameter in both cases, as described in (6.1). A ratio of 30 was chosen between the highest conductivity or permeability value and the lowest one, to obtain a comparable sensitivity estimate. A higher sheet conductivity decreases the sheet resistance and the efficiency, while a higher permeability increases the efficiency as predicted in (6.2).

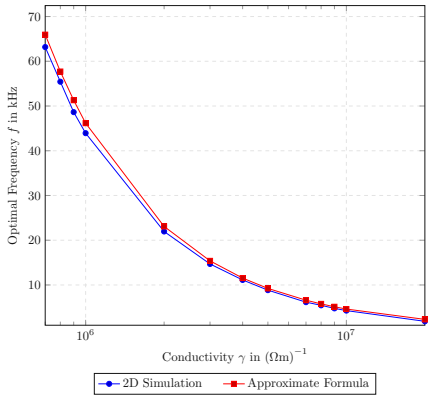

(a) Optimal frequency.

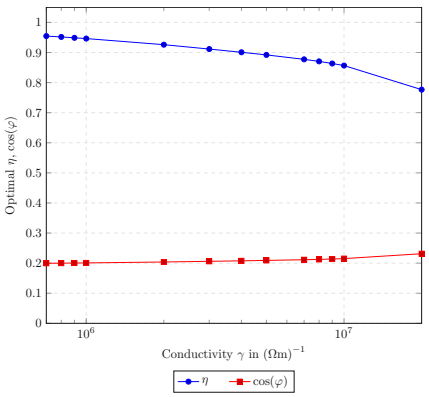

(b) Efficiency and power factor at optimal frequency.

Figure 6.3: Influence of conductivity γ on efficiency for LFH.

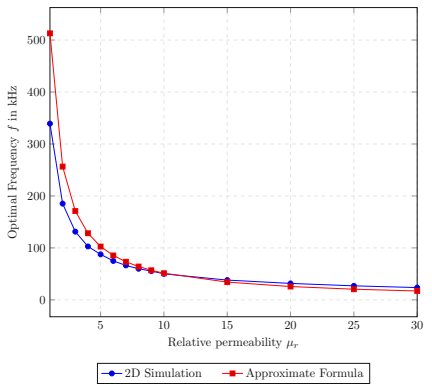

(a) Optimal frequency.

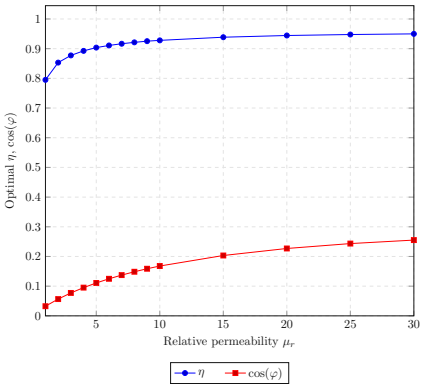

(b) Efficiency and power factor at optimal frequency.

Figure 6.4: Influence of relative permeability μ_r on efficiency for LFH.

6.2 Transverse Flux Heating

6.2.1 Parameter studies

The relevant geometry parameters for TFH have been known since the 1940s [5]. As the conventions are slightly different from the ones chosen in Fig. 5.1, new reference dimensions in accordance with TFH literature are defined in Fig. 6.5, namely the pole pitch t and the height of the air gap h_{gap}. The sheet thickness d and the inductor width b_{ind} are measured as before. If not stated differently, the default parameters from Tab. 6.1 are used.

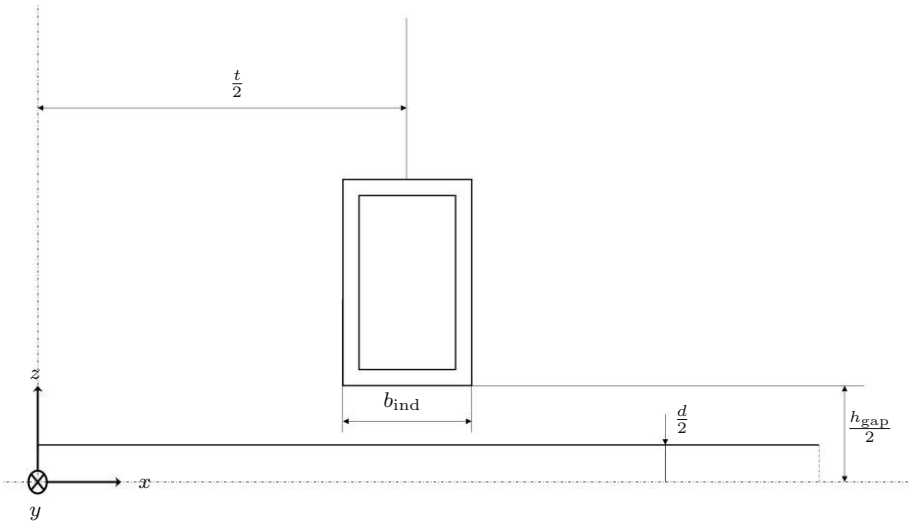

Figure 6.5: Setup with all relevant geometric dimensions.

Table 6.1: Reference Dimensions TFH, dimensions defined as in Fig. 6.5, all dimensions in mm.

Name Symbol	Pole pitch t	Air gap h_{gap}	Inductor Width b_{ind}	Sheet thickness d
Value	150	20	15	1.5

Various empirical formulas for the optimal frequency can be found in literature, but unfortunately they are valid only for a very specific combination of parameters and do not take into account all geometry influences [47] [24]. A reasonable first estimate of the efficient frequency can be found in [47],

$$f_{\text{opt}} \approx \frac{1.52}{\mu_0 \gamma d t}. \tag{6.3}$$

For $d/\delta << 1$, the current in the sheet is mainly induced by the normal (transverse) magnetic flux density between the inductors as shown in Fig. 5.18(b). According to Faraday's law, the induced tension in the sheet depends on

$$U_{\text{ind}} = -\frac{N d\Phi}{dt}, \tag{6.4}$$

where $N = 2$ for both-sided inductors and Φ denotes the total magnetic flux defined by the surface integral $\Phi = \int_S \boldsymbol{B} \cdot d\boldsymbol{S}$. Considering the 2 inductors as 2 parallel circular current loops having a radius of half the pole pitch $t/2$, the total inductance $L = \frac{N\Phi}{I}$ is given by

$$L = \frac{\pi}{2} \mu_0 \frac{t}{2}, \tag{6.5}$$

under the assumption that $\frac{t}{2} >> h_{\text{gap}}$ [52]. This expression is also valid for the case of an iron core between the current loops with a correction factor for the higher flux, so the presence of the sheet should not affect the qualitative behaviour. So for the same current I, a higher pole pitch increases the efficiency and power factor as can be seen in Fig. 6.6(b). The optimal frequency behaves as predicted by (6.3).

If the assumption for $\frac{t}{2} >> h_{\text{gap}}$ is no longer satisfied, (6.5) is changed to [52]

$$L = \frac{\pi}{2} \mu_0 \frac{t^4}{16 h_{\text{gap}}^3}. \tag{6.6}$$

Therefore, the induced current in the sheet will be reduced for high values of h_{gap}. Moreover, the stray losses and return path losses will increase. For a single-sided inductor the principle is the same as for the current filament described in Sec. 4.3. This explains the decrease of efficiency and power factor in Fig. 6.7 for higher values of h_{gap}.

Given that the electric current density is almost constant over the sheet thickness below the inductor, as observed in Sec. 5.2.2, the sheet resistance will depend on $\frac{1}{db_{\mathrm{ind}}}$. This results in the efficiency decrease for larger sheet thicknesses seen in Fig. 6.8(b). Through the analytical considerations in Sec. 4.2 no optimal d/δ ratio could be found, still it is evident that the transverse flux configuration is only obtained for ratios d/δ well below 1 where the sheet is sufficiently transparent to the magnetic flux in vertical direction. Hence, the optimal frequency in Fig. 6.8(a) must decrease for sheets of higher thickness, which also agrees with (6.3). The efficiency increase for larger inductors in Fig. 6.9 cannot be explained by considering the sheet resistance. In fact, when evaluating the total efficiency according to (4.1), there is no direct dependency on b_{ind} because it appears both in the expression for R_{sheet} and R_{ind}. In contrast, a bigger inductor width decreases the stray losses, as the field lines in the air gap will be conducted through the air over longer distances [47], leading to a smaller stray flux.

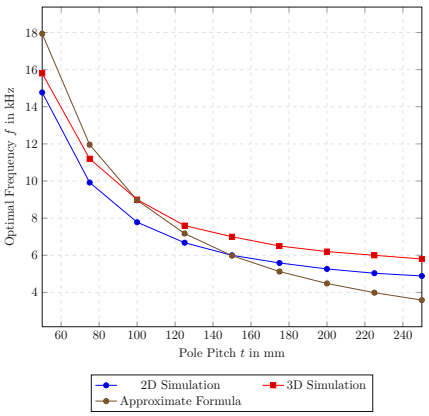

(a) Optimal frequency.

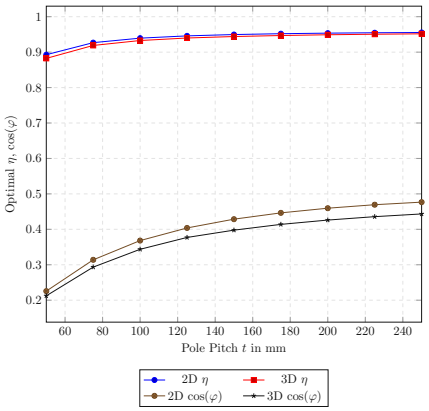

(b) Efficiency and power factor at optimal frequency.

Figure 6.6: Influence of pole pitch t on efficiency for TFH.

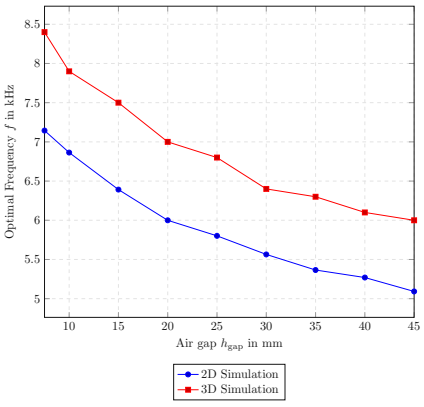

(a) Optimal frequency.

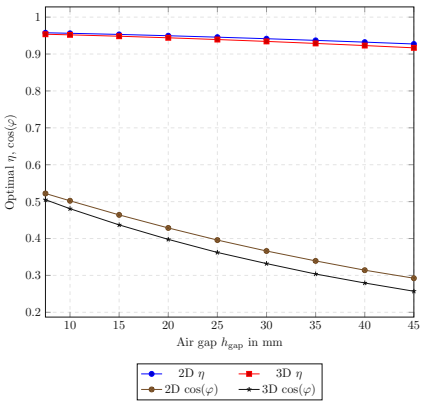

(b) Efficiency and power factor at optimal frequency.

Figure 6.7: Influence of air gap h_{gap} on efficiency for TFH.

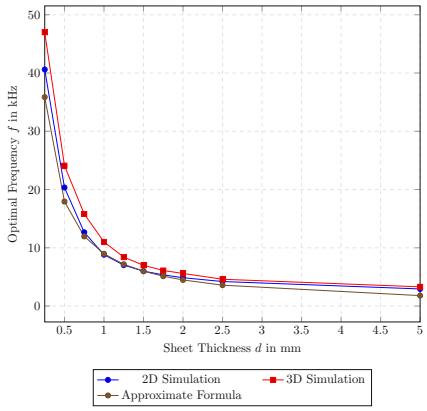

(a) Optimal frequency.

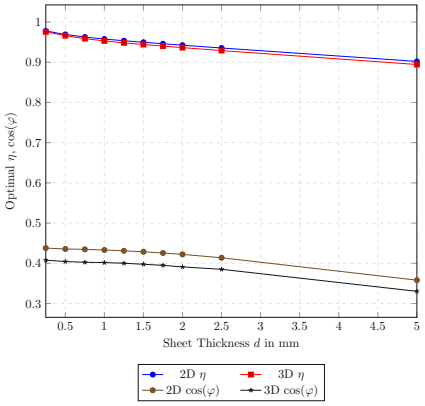

(b) Efficiency and power factor at optimal frequency.

Figure 6.8: Influence of sheet thickness d on efficiency for TFH.

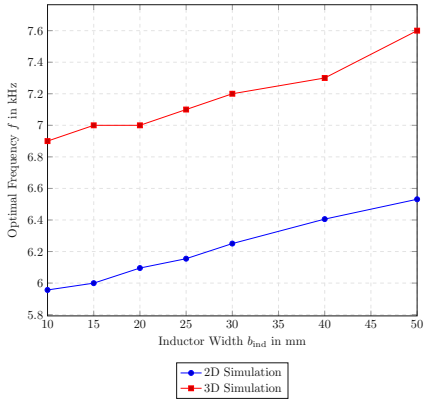

(a) Optimal frequency.

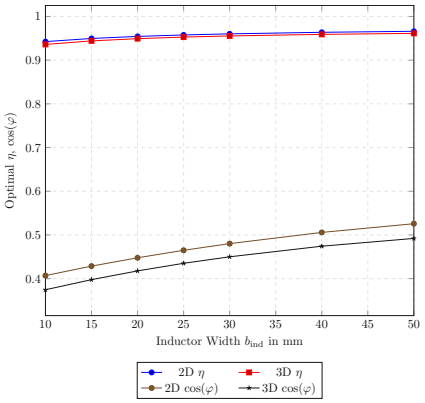

(b) Efficiency and power factor at optimal frequency.

Figure 6.9: Influence of inductor width b_{ind} on efficiency for TFH.

Regarding the agreement between the 2D and 3D simulations, it can be concluded that even if there are significant insecurities in the prediction of the optimal frequency with the 3D values always 10-20% higher than their 2D equivalent, the prediction of the maximum electrical efficiency is quite accurate with less than 1.5% maximum absolute deviation over the whole considered parameter range. More importantly, when evaluating the 3D efficiency at the optimal frequency predicted by the 2D computations, absolute differences of only 0.8-1.5% are obtained. Around the optimal frequency, the electrical efficiency is almost constant over a wide range of frequency values, so even for large differences in frequency, the efficiency variation can still be small. For the power factor the maximum is more pronounced, with a more important decrease for frequency values higher than the maximum. In consequence, the deviation from the 2D prediction is higher, reaching up to 3.5%. In general, the lower efficiency of the 3D setup is due to the increased losses in the turn. According to Fig. 5.15, the power factor is stronger affected by this.

As discussed in Sec. 5.2.2, the maximum of the power factor ($\cos(\varphi)$ criterion) does not exactly coincide with the maximum of the the electrical efficiency (η criterion). This question was analyzed using two-dimensional simulations in Fig. 6.10, for different pole pitches and different sheet thicknesses. The variation of the optimal frequency over the pole pitch is higher for the η criterion than for the $\cos(\varphi)$ criterion, a result that was also found in Ref. [25]. For the case studied in Ref. [25] with a sheet thickness of 0.8mm, there is a similar intersection of the frequency curves as for d =0.75mm in Fig. 6.10(a). In general, the difference in the frequency and efficiency results between the two different criteria increase in cases with low electrical efficiency.

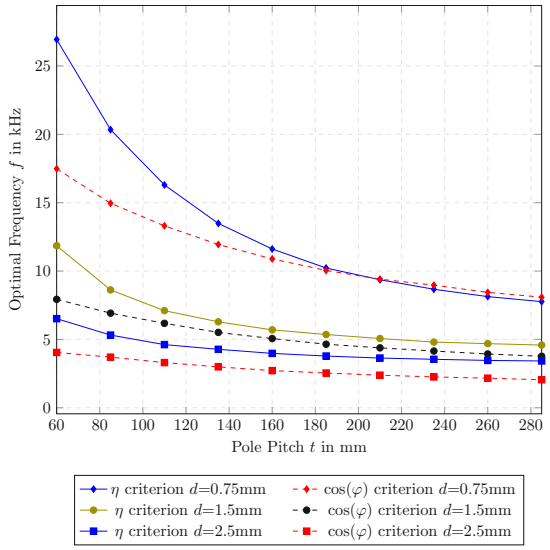

(a) Optimal frequency for different criteria.

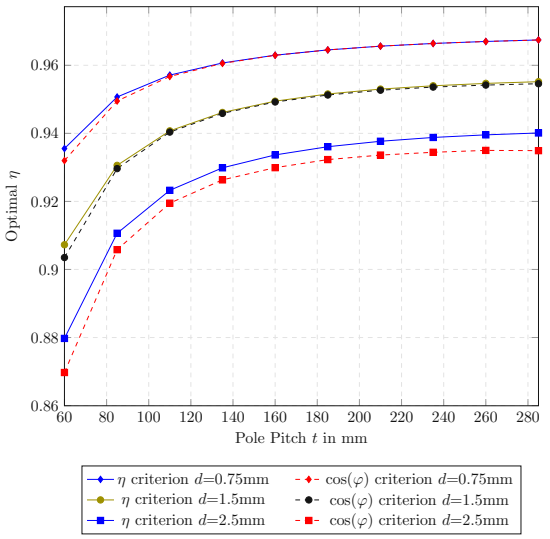

(b) Efficiency at optimal frequency for different criteria.

Figure 6.10: Comparison of differences between frequency of maximum efficiency (η criterion) and frequency of maximum power factor ($\cos(\varphi)$ criterion) for different pole pitches t and different sheet thickness d for TFH.

The dependency on the material parameters is only studied for the 2D case. For the influence of the conductivity on the optimal efficiency, a similar relation as for the LFH case applies [47],

$$\eta_{\text{opt}} \sim \frac{1}{1+\sqrt{\frac{\gamma}{\gamma_{\text{i}}}}}. \tag{6.7}$$

This agrees well with the efficiency decrease in Fig. 6.11(a), while the behaviour of the optimal frequency Fig. 6.9(b) is also described reasonably well by the empirical formula (6.3). A special property of TFH is that the efficiency changes in a certain frequency range around the optimal frequency are small and that within these frequencies it is not sensitive to changes in the magnetic permeability of the material [3]. For an increase of the relative permeability from 1 to 30 in Fig. 6.12, the change of the optimal frequency is only 12.5%, while for an increase by the same factor of the electric conductivity, the optimal frequency is divided by a factor 7. Similarly, the diminution in maximum efficiency is below 1%, which agrees well with the results found in literature, e.g., in [53].

Only linear material parameters have been considered in the above parameter studies. Relevant nonlinearities in the context of the optimal frequency are the hysteretic B-H curve as well as the temperature dependency of the electric conductivity and the permeability.

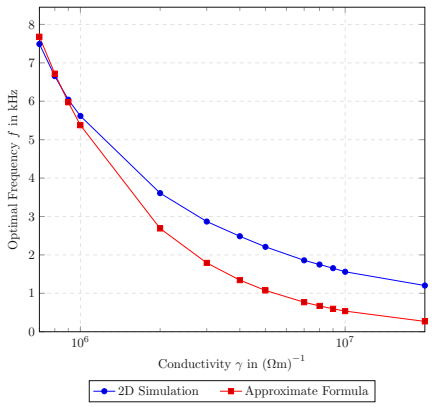

(a) Optimal frequency.

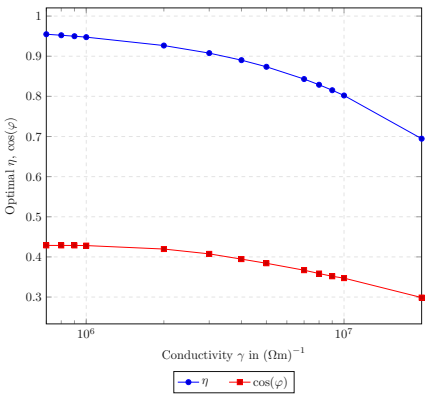

(b) Efficiency and power factor at optimal frequency.

Figure 6.11: Influence of conductivity γ on efficiency for TFH.

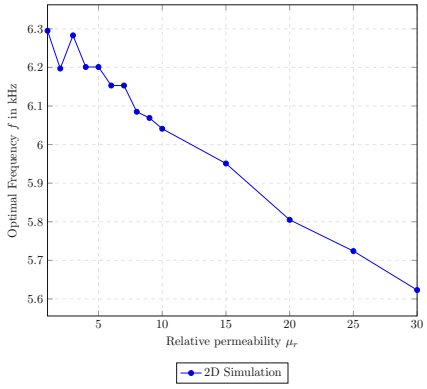

(a) Optimal frequency.

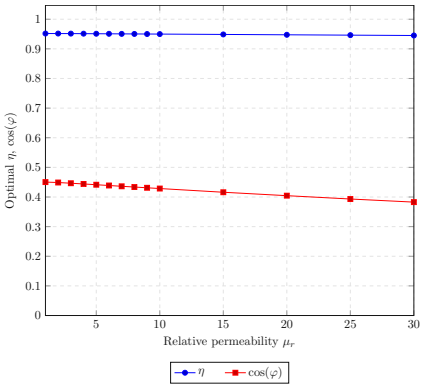

(b) Efficiency and power factor at optimal frequency.

Figure 6.12: Influence of relative permeability μ_r on efficiency for TFH.

For metals, the linear temperature coefficient for the electric resistivity α is in the range 0.0015 to 0.006 [54], so for maximum temperature increases around 1000°C, one can expect a significant increase in the sheet resistance, which will also have an impact on the efficiency results. When temperatures near the Curie point of the material are reached, a drop of the permeability to $\mu_r = 1$ occurs [55]. In addition to the material nonlinearities, the inhomogenous temperature field, as well as the magnetic forces will lead to mechanical deformations in the TFH case, changing the coupling height and thus also affecting the efficiency. To evaluate the fully nonlinear magnetic-thermal-mechanic coupling, the operating point, namely input power and frequency, must be known. It is determined by the desired temperature profile and not always known in the early design stage. Hence, a determination of the optimal frequency including all non-linearities is barely possible, besides the fact that the computational cost of evaluating all these iterative couplings over a wide frequency range will quickly become prohibitive.

Simulation results for TFH taking into account material nonlinearities in [55] and [56] lead to the following conclusions: As already suggested by 6.12, the results are not sensitive to changes in the magnetic permeability. Therefore, sheets of different permeabilities can be heated without any adjustments of the equipment. However, a strong influence of the conductivity changes can be expected, so once the operating point is known, the efficiency results should be counter-checked using a temperature dependent conductivity.

6.2.2 Presence of a Core

The inductors can be embedded in a magnetic yoke, that with its higher magnetic permeability reduces the reluctances in the magnetic circuit and leads to a higher magnetic flux. While for highly conducting materials such as aluminum or copper, satisfactory efficiencies can only be achieved using a core, the sheets with moderate conductivity treated in this thesis can also be heated using a setup without flux concentrators [47]. Nevertheless, a comparison of the dependency of efficiency and optimal frequency with and without the presence of a core will be given in the following.

From a direct comparison of the efficiency curves in Fig. 6.13, it follows that the optimal frequency for the case without core is about twice as high as in the setup with core, as stated in [47]. For the electrical efficiency, there is no significant difference, but the power factor is about 20% higher.

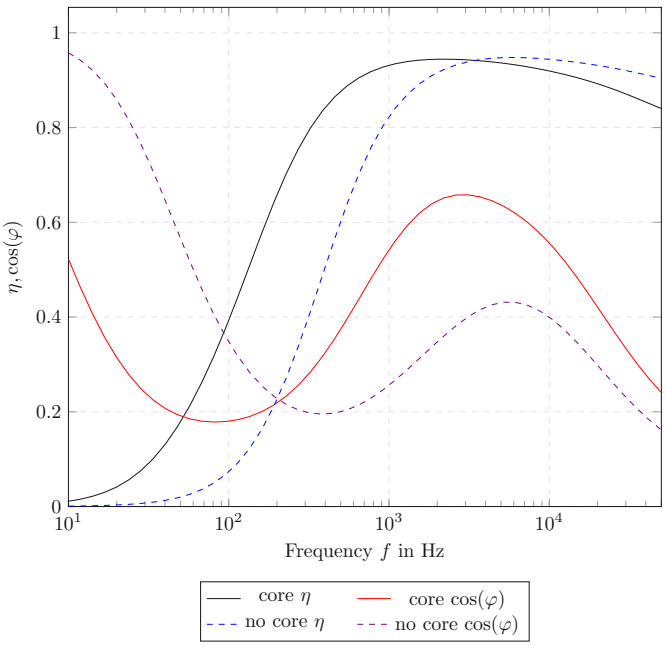

Figure 6.13: Comparison of the influence of a magnetic core on the curves for electrical efficiency η and power factor $\cos(\varphi)$ over the excitation frequency for TFH. Optimal frequency: with core: 2.25kHz, without core: 6.02KHz.

For the setup with a core in Fig. 6.14(a), the magnetic flux will be strongly concentrated between the inductors, which can be seen from the induced current profile in the sheet depicted in Fig. 6.14(b), where the current is strongly concentrated below the conductors in the case with core. Hence, return path losses become negligible and stray losses are reduced [47], which explains the huge difference in the power factor values.

In all parameter studies 6.15-6.18, the qualitative dependency, of the efficiency values is the same with or without core and the previous explanations remain valid. Overall, the optimal frequency is approximately twice as high for the setup without core and there is a significant difference in the maximum power factor value while the efficiency differences are very small. For the influence of pole pitch and sheet thickness, Fig. 6.15 and Fig. 6.17 respectively, the behaviour of the optimal frequency is also the same. However, for the case of an increasing air gap height in Fig. 6.7(a), the optimal frequency decreases for the case without core and increases for the case with core. Similar results can be found in literature, comparing, e.g., [5] for the setup with core and [3] for a sensitivity study without core. As already mentioned, a larger air gap leads to a lower magnetic flux through the sheet, while simultaneously causing higher stray and return path losses.

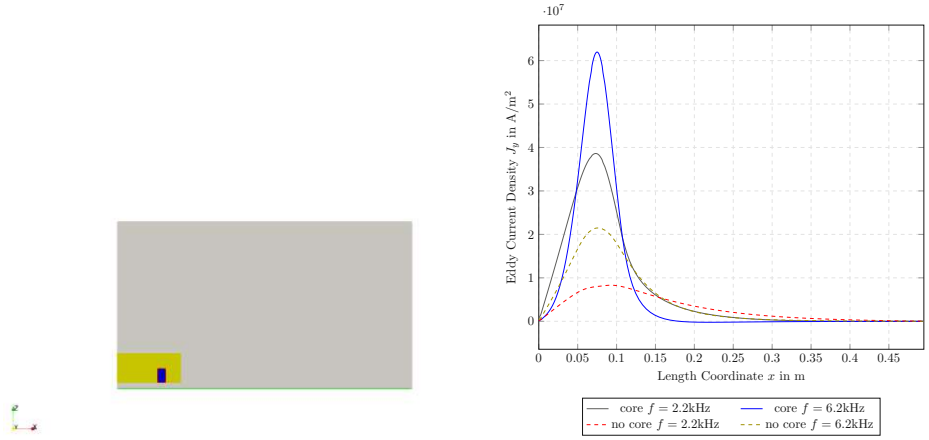

(a) Geometry of the TFH setup with magnetic core (core in yellow).

(b) Influence of the magnetic core on the eddy current density distribution at the surface over the sheet length.

Figure 6.14: TFH Setup with core.

Due to the concentration of the magnetic flux by the core, there will be a fundamentally different weighting of these effects as compared to the case without core, which can lead to an inverse efficiency trend. Varying the inductor width b_{ind} Fig. 6.18, the frequency is almost constant for the case with core, but increases for the case without core. It should also be noted that there is a minor influence of the coupling height h_{coupling} and inductor width b_{ind} on the frequency as compared to a change in pole pitch or sheet thickness. In particular, these parameters are not contained in the empirical formula (6.3), so it can be expected that their influence is either difficult to quantify in a universal way or that it can be neglected in comparison to other parameters.

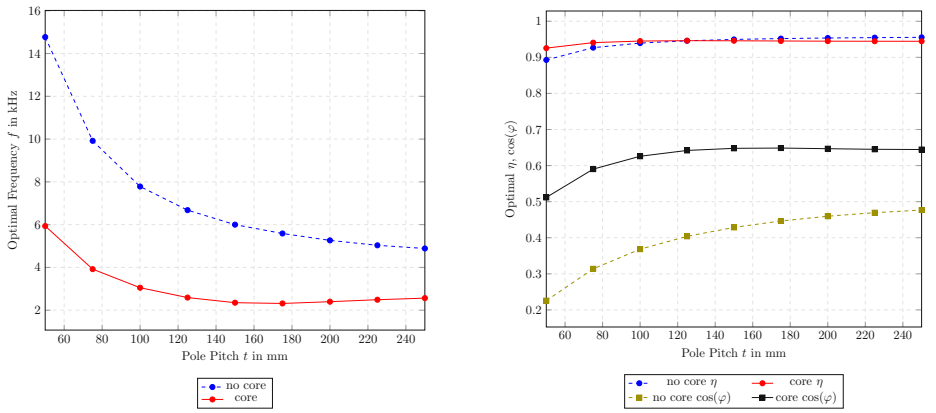

(a) Optimal frequency.

(b) Efficiency and power factor at optimal frequency.

Figure 6.15: Influence of pole pitch t on efficiency for TFH, with and without magnetic core.

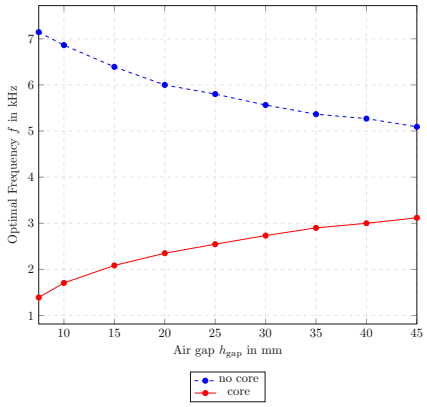

(a) Optimal frequency.

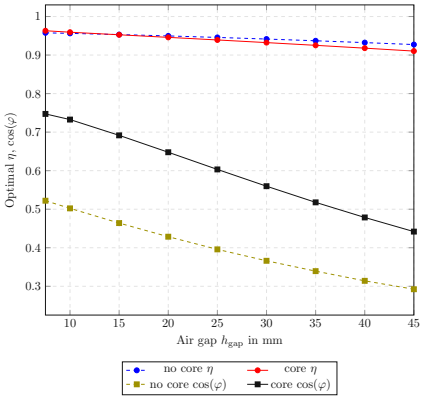

(b) Efficiency and power factor at optimal frequency.

Figure 6.16: Influence of air gap h_{gap} on efficiency for TFH, with and without magnetic core.

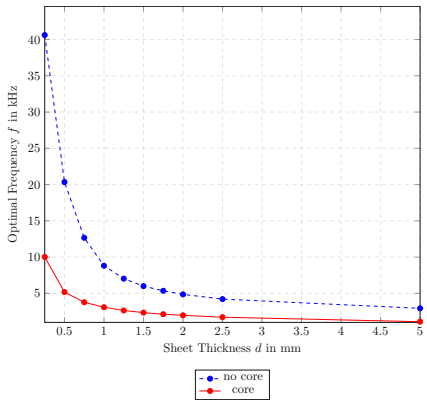

(a) Optimal frequency.

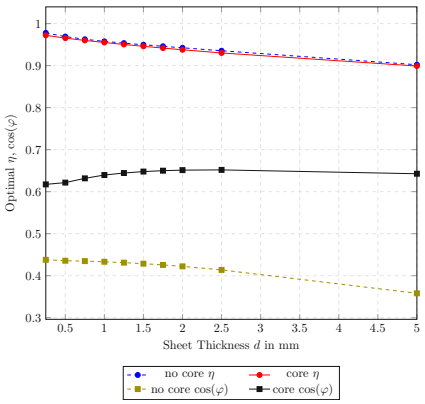

(b) Efficiency and power factor at optimal frequency.

Figure 6.17: Influence of sheet thickness d on efficiency for TFH, with and without magnetic core.

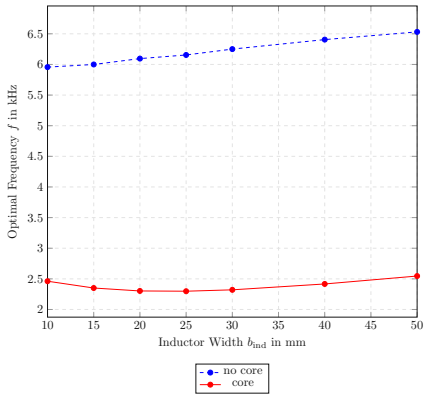

(a) Optimal frequency.

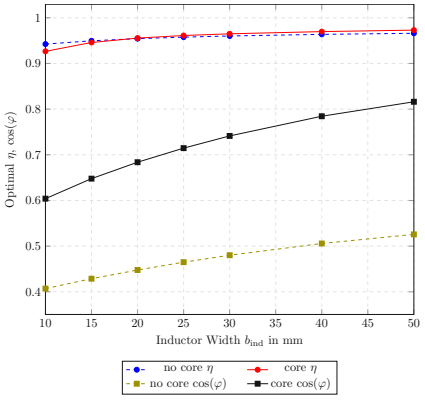

(b) Efficiency and power factor at optimal frequency.

Figure 6.18: Influence of inductor width b_{ind} on efficiency for TFH, with and without magnetic core.

6.2.3 Multiple Conductors

In Fig. 6.9, it could be shown that better efficiency results can be achieved when choosing a higher inductor width b_{ind}. However, conductors with high width to height ratios cannot be used in real setups because the required bending radius cannot be realized. One has to subdivide the single conductor into several smaller conductors. In terms of heating power conveyed to the sheet this does not make much difference, but for efficiency considerations, the resistance of the inductor is of high importance and it depends on the aspect ratio of the rectangular cross section, as discussed in Sec. 4.1. In the following, we will compare a setup with a single conductor to a setup with three separate conductors and investigate to what extent the results found for the single inductor can be applied to multiple inductors.

For the considered example, a single conductor of width $b_{\text{ind}} = 50\text{mm}$, excited by a current of $\hat{I} = 2.5\text{kA}$, was subdivided into three conductors of width $b_{\text{ind}} = 15\text{mm}$ with a current of $\hat{I} = 0.833\text{kA}$. The wall thickness is the same in both cases, $t_{\text{ind}} = 1.5\text{mm}$. Of course, this is not exactly equivalent, because the total conducting surface area will be different in the two cases, but modifying the wall thickness would also affect the results, so we assume that the comparison is representative nonetheless.

For the direct comparison of the efficiency curves Fig. 6.19, it can be concluded that the differences from an optimal frequency point of view are very small and also the maximum electrical efficiency for the multiple conductor case is only 1% lower. The lower efficiency can be explained by a resistance increase due to the proximity effect [57]. This effect causes a redistribution of the current density in the conductor due to the electromagnetic field of other nearby conductors carrying an AC [1]. The differences in the power factor are more pronounced: in the optimal frequency range, the curve of the single conductor is located between the three curves of the multi-conductor setup, where the middle conductor has the lowest power factor, while the power factor curves of the outer conductors are practically overlapping over the entire frequency range. The proximity effect is responsible for the lower power factor in the middle conductor: for two conductors with currents flowing in the same direction, the maximum current density occurs on the far-side of the conductors, with a minimum on the faces in front of each other [1] as visualized in Fig. 6.20. In the case of three conductors, this will imply a higher phase-shift for the middle conductor, explaining its lower power factor.

Another important point are edge effects: from Fig. 6.20(a) it can be seen that the current density is concentrated at the edges of the rectangular conductor, which was already discussed in Sec. 4.1. In the part of the cross section far away from the edges, there is no gradient in circumferential direction but only in thickness direction. For the multi-conductor case in Fig. 6.20(b), there is a superposition of the proximity effect and edge effects, so the maxima are less pronounced for the inner edges.

According to Fig. 6.21, the resulting inhomogeneous current distribution over the inductor width causes a peak in the induced sheet current density for the multi-conductor case, when comparing it to the single-conductor setup. All in all, it can be concluded that the single conductor case offers a good estimate for the efficiency parameters of the multi-inductor setup, but if the exact current distribution over the inductor width is needed, the additional inductor cross sections should be modelled.

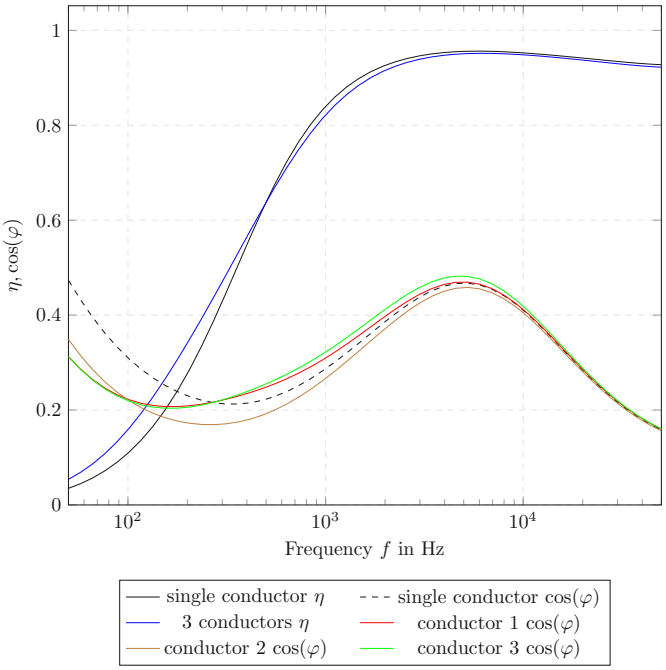

Figure 6.19: Comparison of the influence of the division of the single conductor into several ones on the curves for electrical efficiency η and power factor cos(φ) over the excitation frequency for TFH. Optimal frequency: single conductor: 6.51KHz, multiple conductors 6.55KHz.

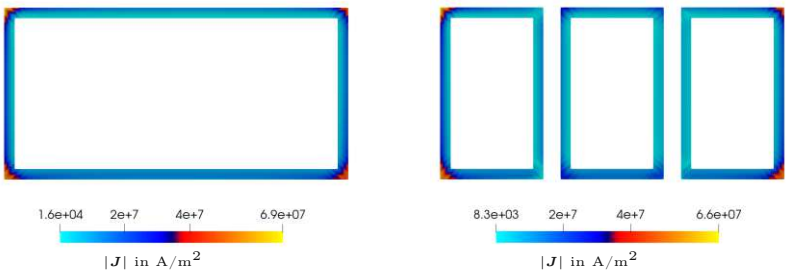

(a) Eddy current density magnitude in single conductor.

(b) Eddy current density magnitude in 3 conductors.

Figure 6.20: Comparison of the eddy current density distribution between the setup with a single conductor and its subdivision into 3 conductors.

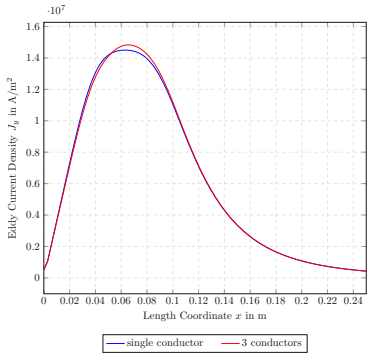

Figure 6.21: Comparison of eddy current density over sheet length at f=6.5KHz.

Chapter 7

Conclusion and Outlook

In this thesis, the question of the optimal excitation frequency for the two most important induction heating setups for metal sheets, longitudinal flux heating and transverse flux heating, has been analyzed. Numerical results found by the Finite Element Method have been used to obtain efficiency curves over a wide frequency range and derive the optimal frequency. Furthermore, the dependency of the optimal frequency on various relevant parameters could be validated using analytical models and empirical formulas from literature. In the following, the results of this thesis will be discussed from the point of view of the design process of induction heating applications.

Two-dimensional simulations are computationally efficient and yield usable estimates for the optimal frequency, the maximum electrical efficiency and the power factor. On a standard notebook, finding the optimal efficiency for an arbitrary two-dimensional setup takes barely 2 minutes, with a maximum memory consumption of 500MB. For longitudinal flux heating, it could be shown that the efficiency curves for the two-dimensional and three-dimensional computations are practically overlapping, since there are no significant three-dimensional effects in that case. By contrast, for transverse flux heating, the turning of the sheet current along the edge leads to eddy current concentrations and deviations from the two-dimensional current profile. As a consequence, the optimal frequency for the three-dimensional case is up to 20% higher than the value obtained by two-dimensional computations. Nevertheless, the prediction of the maximum efficiency value is sufficiently accurate with deviations of less than 2% for the studied parameter range. Furthermore, for the determination of the optimal frequency, material nonlinearities and mechanical deformations are neglected because the evaluation of the iterative couplings for a full three-dimensional model over a wide frequency range is computationally too expensive. Additionally, when assessing the accuracy of the frequency prediction, one has to take into account the coil-supply system. In fact, in induction heating installations, the coils are supplied by resonant inverters, consisting of thyristors, MOSFET or IGBT switches and also contain a capacitor bank to compensate the reactive power required by the coil [24]. Thus, the resonant frequency also depends on this capacitance, so that in general it is not possible to prescribe arbitrary values of the excitation frequency. To conclude, we can say that in an initial design phase, the optimal frequency obtained by linear two-dimensional computations is sufficient. In most cases, technical specifications of the electrical system, as well as unknown disturbances in the real plant, such as the influence of metal supports on the magnetic field or changes in the temperature of the surrounding air, will cause higher deviations than those induced by reducing the complexity of the computational model.

Once the optimal frequency is known, the coupled magnetic-thermal problem can be solved for the full three-dimensional model taking into account all relevant material nonlinearities to get a realistic prediction of the temperature distribution in the sheet. For transverse flux heating setups with high power densities and large temperature gradients, the mechanical deformations should also be evaluated.

In the last two chapters, especially for transverse flux heating, it was shown that there is a strong dependency of the efficiency on geometry parameters, e.g., pole pitch or bend position. In order to realize a well-designed setup, combining a high electrical efficiency and a homogeneous temperature distribution, it can be advantageous to formulate a constrained optimization problem for several parameters and not only the excitation frequency. The objective functions to be minimized can be either efficiency based or enforce a certain temperature profile. A large number of optimization techniques for induction heating problems has been developed to which a good introduction can be found in [58] and [59]. Nonetheless, the results from this thesis are a prerequisite for the formulation of suitable constraints on the frequency.

Bibliography

[1] S. Lupi. *Fundamentals of Electroheat : Electrical Technologies for Process Heating*. Springer International Publishing, 2017.

[2] O. Lucía, P. Maussion, E. J. Dede, and J. M. Burdío. "Induction heating technology and its applications: past developments, current technology, and future challenges". *IEEE Transactions on industrial electronics*, 61(5):2509–2520, 2013.

[3] M. Schulze, A. Nikanorov, and B. Nacke. "Hierarchical shape optimization of one-sided transverse flux heating induction coil". *COMPEL-The international journal for computation and mathematics in electrical and electronic engineering*, 39(1):73–80, 2020.

[4] R. M. Baker. "Heating of nonmagnetic electric conductors by magnetic induction—Longitudinal flux". *Electrical Engineering*, 63(6):273–278, 1944.

[5] R. M. Baker. "Transverse flux induction heating". *Electrical Engineering*, 69(10):922–924, 1950.

[6] openCFS. `https://www.opencfs.org/`. Accessed: 2023-07-01.

[7] M. Kaltenbacher. *Numerical Simulation of Mechatronic Sensors and Actuators*. Springer-Verlag, 2007.

[8] K. Roppert. *Modelling and Numerical Simulation of Induction Heating Processes for Thin Steel Sheets*. Phd thesis, Technische Universität Wien, 2020.

[9] J. C. Maxwell. *A treatise on electricity and magnetism*, volume 1. Oxford: Clarendon Press, 1873.

[10] L. Nickelson. *Electromagnetic Theory and Plasmonics for Engineers*. Springer Singapore, 2019.

[11] M. Bartelmann, B. Feuerbacher, T. Krüger, D. Lüst, A. Rebhan, and A. Wipf. *Theoretische Physik 2 / Elektrodynamik*. Springer Berlin Heidelberg, 2018.

[12] R. Hiptmair and O. Sterz. "Current and voltage excitations for the eddy current model". *International Journal of Numerical Modelling: Electronic Networks, Devices and Fields*, 18(1):1–21, 2005.

[13] J. A Tegopoulos and E. E Kriezis. *Eddy currents in linear conducting media*. Studies in electrical and electronic engineering. Elsevier Amsterdam, 1985.

[14] C. Gerthsen, D. Meschede, and H. Vogel. *Gerthsen Physik*. Springer-Lehrbuch. Springer Spektrum, 25. auflage edition, 2015.

[15] B. Nacke. *Induktives Erwärmen*. Vulkan Verlag Essen, 2014.

[16] H. D. Baehr and K. Stephan. *Wärme- und Stoffübertragung*. Springer Vieweg, Berlin, 2019.

[17] Z Wang, W Huang, W Jia, Q Zhao, Y Wang, W Yan, D Schulze, G Martin, and U Luedtke. "3D multifields FEM computation of transverse flux induction heating for moving-strips". *IEEE transactions on magnetics*, 35(3):1642–1645, 1999.

[18] P. Wesseling. *Principles of Computational Fluid Dynamics*. Springer series in computational mathematics. Springer, 2001.

[19] E. Ter Maten and J. Melissen. "Simulation of inductive heating". *IEEE transactions on magnetics*, 28(2):1287–1290, 1992.

[20] IEEE. "IEEE Standard Definitions for the Measurement of Electric Power Quantities Under Sinusoidal, Nonsinusoidal, Balanced, or Unbalanced Conditions". *IEEE Std 1459-2010 (Revision of IEEE Std 1459-2000)*, pages 1–50, 2010.

[21] DIN. "DIN 40110-1:1994-03:Wechselstromgrößen; Zweileiter-Stromkreise". *DIN*, pages 1–14, 1994.

[22] N. R. Stansel. "Induction heating—Selection of frequency". *Electrical Engineering*, 63(10):755–759, 1944.

[23] D. Wohlfahrt and R. Jürgens. "Induction heating of thin slabs and sheets in the rolling line". In *Information technology and electrical engineering-devices and systems, materials and technologies for the future*, volume 51, 2006.

[24] A. Spagnolo. *Auto-adaptive Multi-coil Inductors for Transverse Fluid Induction Heating of Metal Strips*. Phd thesis, Padua University, 2011.

[25] F. Dughiero, S. Lupi, A. Mühlbauer, and A. Nikanorov. "TFH-transverse flux induction heating of non-ferrous and precious metal strips: Results of a EU research project". *COMPEL-The international journal for computation and mathematics in electrical and electronic engineering*, 22(1):134–148, 2003.

[26] A. Bossavit and I. Mayergoyz. *Computational Electromagnetism : Variational Formulations, Complementarity, Edge Elements*. Electromagnetism. Academic Press, San Diego, 1st edition edition, 1998.

[27] R. A. Adams and J. F. Fournier. *Sobolev Spaces*. Pure and applied mathematics ;. Academic Press, Amsterdam, 2nd ed. edition, 2003.

[28] Michel Cessenat. *Mathematical Methods in Electromagnetism: Linear Theory and Applications*. World Scientific, 1996.

[29] P. J. Leonard and D. Rodger. "Comparison of methods for modelling jumps in conductivity using magnetic vector potential based formulations". *IEEE Transactions on Magnetics*, 33(2):1295–1298, 1997.

[30] M. Koshiba, K. Hayata, and M. Suzuki. "Finite-element formulation in terms of the electric-field vector for electromagnetic waveguide problems". *IEEE transactions on microwave theory and techniques*, 33(10):900–905, 1985.

[31] G. Mur. "Edge elements, their advantages and their disadvantages". *IEEE transactions on magnetics*, 30(5):3552–3557, 1994.

[32] M. Kaltenbacher and S. Reitzinger. "Appropriate finite-element formulations for 3-D electromagnetic-field problems". *IEEE transactions on magnetics*, 38(2):513–516, 2002.

[33] J.-C. Nédélec. "Mixed finite elements in R3". *Numerische Mathematik*, 35:315–341, 1980.

[34] H. Igarashi. "On the property of the curl-curl matrix in finite element analysis with edge elements". *IEEE transactions on magnetics*, 37(5):3129–3132, 2001.

[35] M. R. Dorr. "On the discretization of interdomain coupling in elliptic boundary-value problems". *Domain decomposition methods*, pages 17–37, 1989.

[36] J. Nitsche. "Über ein Variationsprinzip zur Lösung von Dirichlet-Problemen bei Verwendung von Teilräumen, die keinen Randbedingungen unterworfen sind". In *Abhandlungen aus dem mathematischen Seminar der Universität Hamburg*, volume 36, pages 9–15. Springer, 1971.

[37] B. Flemisch, M. Kaltenbacher, and B. Wohlmuth. "Elasto–acoustic and acoustic–acoustic coupling on non-matching grids". *International Journal for Numerical Methods in Engineering*, 67(13):1791–1810, 2006.

[38] O. Bíró. "Edge element formulations of eddy current problems". *Computer methods in applied mechanics and engineering*, 169(3-4):391–405, 1999.

[39] A. Mühlbauer. *History of Induction Heating and Melting*. Vulkan Verlag Essen, 2008.

[40] K. Schönbacher. "Zur Berechnung von Induktionsöfen". *ETZ A*, pages 736–738, 1952.

[41] R. M. Baker. "Design and calculation of induction-heating coils". *Transactions of the American Institute of Electrical Engineers, Part II: Applications and Industry*, 76(1):31–40, 1957.

[42] A. Ametani and I. Fuse. "Approximate method for calculating the impedances of multiconductors with cross sections of arbitrary shapes". *Electrical Engineering in Japan*, 112(2):117–123, 1992.

[43] P. L. Dowell. "Effects of eddy currents in transformer windings". In *Proceedings of the Institution of electrical Engineers*, volume 113-8, pages 1387–1394. IET, 1966.

[44] B. Tabei, A. Ametani, A. Gole, and B. Kordi. "Quasi-analytical calculation of frequency-dependent resistance of rectangular conductors considering the edge effect". *Energies*, 15(2):503, 2022.

[45] N. H. Kutkut. "A simple technique to evaluate winding losses including two-dimensional edge effects". *IEEE Transactions on Power Electronics*, 13(5):950–958, 1998.

[46] X. Wang, L. Wang, L. Mao, and Y. Zhang. "A simple analytical technique for evaluating the 2-D conductive losses in isolated rectangular conductor". In *2019 IEEE Applied Power Electronics Conference and Exposition (APEC)*, pages 1245–1249. IEEE, 2019.

[47] G. Nauvertat. *Optimiertes Design industrieller induktiver Querfeld-Banderwärmungsanlagen*. Phd thesis, Universität Hannover, 2003.

[48] E. Horoszko. "Induction heating of flat objects". *Archiv für Elektrotechnik*, 57:133–143, 1975.

[49] H. Poritsky and R. P. Jerrard. "Eddy-current losses in a semi-infinite solid due to a nearby alternating current". *Transactions of the American Institute of Electrical Engineers, Part I: Communication and Electronics*, 73(2):97–106, 1954.

[50] M. Papageorgiou, M. Leibold, and M. Buss. *Optimierung*, volume 4. Springer, 2015.

[51] V. Demidovich, Y. Perevalov, and O. Demidovich. "Numerical Simulation of Induction Heating of Steel Plate Products". In *International Symposium" Engineering and Earth Sciences: Applied and Fundamental Research"(ISEES 2018)*, pages 173–177. Atlantis Press, 2018.

[52] W. Demtröder. *Experimentalphysik 2 : Elektrizität und Optik*. Springer-Lehrbuch. Springer Berlin Heidelberg, 6., überarb. u. akt. aufl. 2013 edition, 2013.

[53] M. Jestremski, H. Schülbe, A. Nikanorov, and B. Nacke. "Numerical Investigation of Transverse-Flux Induction Heating of Ferromagnetic Strip". *International Journal of Business Continuity & Risk Management*, 7(2):359–368, 2017.

[54] H. Dubbel and K.-H. Grote. *Taschenbuch für den Maschinenbau*. Springer Vieweg, 2014.

[55] M. Zlobina, S. Galunin, Y. Blinov, B. Nacke, A. Nikanorov, and H. Schülbe. "Numerical modelling of non-linear transverse flux heating systems". *stainless steel*, 40(45):50, 2003.

[56] A. Nikanorov, H. Schulze, B. Nacke, M. Zlobina, S. Galunin, and Y. Blinov. "Non linear effects in transverse flux heating systems". In *Proc. of HES-04 Seminar*, 2004.

[57] I. Lope, J. Acero, and C. Carretero. "Analysis and optimization of the efficiency of induction heating applications with litz-wire planar and solenoidal coils". *IEEE Transactions on Power Electronics*, 31(7):5089–5101, 2015.

[58] Y Favennec, V Labbé, and F Bay. "Induction heating processes optimization a general optimal control approach". *Journal of computational physics*, 187(1):68–94, 2003.

[59] N. Bianchi and F. Dughiero. "Optimal design techniques applied to transverse-flux induction heating systems". *IEEE transactions on magnetics*, 31(3):1992–1995, 1995.

List of Figures

List of Tables